

Bayesian Target-Vector Optimization for Efficient Parameter Reconstruction

Matthias Plock^a, Anna Andrle^b, Sven Burger^{a,c}, and Philipp-Immanuel Schneider^{a,c}

^a*Zuse Institute Berlin, Takustraße 7, 14195 Berlin, Germany*

^b*Physikalisch-Technische Bundesanstalt (PTB), Abbestr. 2-12, 10587 Berlin, Germany*

^c*JCMwave GmbH, Bolivarallee 22, 14050 Berlin, Germany*

Keywords: *Bayesian target-vector optimization, Bayesian optimization, least-squares, parameter reconstruction, inverse problem, metrology*

Abstract

Parameter reconstructions are indispensable in metrology. Here, one wants to explain K experimental measurements by fitting to them a parameterized model of the measurement process. The model parameters are regularly determined by least-square methods, i.e., by minimizing the sum of the squared residuals between the K model predictions and the K experimental observations, χ^2 . The model functions often involve computationally demanding numerical simulations. Bayesian optimization methods are specifically suited for minimizing expensive model functions. However, in contrast to least-square methods such as the Levenberg-Marquardt algorithm, they only take the value of χ^2 into account, and neglect the K individual model outputs. We introduce a Bayesian target-vector optimization scheme that considers all K contributions of the model function and that is specifically suited for parameter reconstruction problems which are often based on hundreds of observations. Its performance is compared to established methods for an optical metrology reconstruction problem and two synthetic least-squares problems. The proposed method outperforms established optimization methods. It also enables to determine accurate uncertainty estimates with very few observations of the actual model function by using Markov chain Monte Carlo sampling on a trained surrogate model.

1 Introduction

A common task in science and engineering is the fitting of the parameters of a model function, in order to match the outputs of the model to an experimental observation. Often, one has to match K experimental observations simultaneously, which can be done by minimizing the sum of the squared residuals χ^2 between model outputs and experimental observations. Generally this is a non-linear least-squares problem, and is regularly solved by iterative numerical schemes, e.g.,

by the Gauss-Newton method or by the Levenberg-Marquardt algorithm [1, 2, 3].

The models involved in these inverse problems, e.g., in optical metrology [4, 5], are often very costly to evaluate, because they frequently revolve around the solution of differential equations via numerical simulations. In scatterometry for example one solves Maxwell's equations to simulate the scattering process of light off a nanostructured sample [6]. This means that depending on the complexity and size of the numerical model, a single evaluation can take several minutes or more to complete. This can present a problem, as many optimization schemes do not handle expensive model functions in an efficient way. Typically they calculate the parameters of the next iteration based on only a few previous model evaluations, neglecting the information from other evaluations of the optimization history. An additional issue for many model functions is the difficulty of obtaining their derivatives with respect to the model parameters. Optimization schemes such as the Levenberg-Marquardt algorithm require derivatives in order to generate a sampling candidate for the next iteration. Frequently, derivatives are generated by means of a finite differences scheme, which is inefficient and often inaccurate. Therefore, parameter reconstructions in metrology applications can place high demands on computing resources and time. This creates the need for efficient and robust reconstruction methods that make optimal use of energy and time consuming model evaluations.

Bayesian optimization (BO) [7, 8] methods are sequential optimization methods that satisfy the resource requirement, and are therefore an appropriate choice when optimizing expensive black-box model functions. At every BO iteration a stochastic model – most often a Gaussian process (GP) [9] – is trained using all previous observations of the model function. This stochastic model is then used to find input parameters for the next iteration, which, e.g., lead to a large expected improvement over the currently known minimum [10].

Recent studies [11, 12] considered the extension of the BO approach for iteratively solving least-squares problems by training K GPs related to each of the K data channels of the model function. In these works, the approach was successfully applied for problems with $K \leq 20$ channels. Huang et al. [13] applied these

approaches to calibrate the parameters $\mathbf{p} \in \mathbb{R}^N$ of an expensive univariate scalar function $f_{\mathbf{p}}(t)$ to measurements for thousands of times t . In order to reduce the dimensionality of the measurements and the corresponding functional response to only $K = 3$, a functional principal component analysis was applied, based on $10N$ space-filling parameter samples prior to solving the least-square problem. In another study [14] a multi-output GP [15, 16] was used in a non-iterative parameter reconstruction approach. I.e., the GP was trained with a precomputed set of simulation results to directly infer parameter values and uncertainties. This lead to higher reconstruction accuracies than a library lookup method.

In this study we start from the approach taken by Uhrenholt and Jensen [12] to develop an algorithm for iterative parameter reconstruction problems, which often have a large number of data channels K , e.g., a few hundred [17, 18, 19]. We find that this creates two particular challenges. First, BO methods are typically associated with a computational overhead of a few seconds when determining new parameter candidates to sample, which is caused by the training of the surrogate model. Training and evaluating $K \sim 100$ independent Gaussian processes dramatically increases this overhead. We propose to use a shared covariance structure to largely limit the additional overhead. Second, in order to be fast, the scheme approximates the probability distribution of χ^2 as an ordinary non-central chi-squared distribution with K degrees of freedom. This appears to work well for a small number of data channels, as is evident from the results presented in [12]. However, for a large number of degrees of freedom K we find that this leads to a very inefficient optimization scheme, as the probability distribution largely underestimates the probability of finding small χ^2 values. We find that using an *effective* number of degrees of freedom \tilde{K} , which is often much smaller than K , leads to good optimization performance. We propose to choose the value of \tilde{K} with maximum-likelihood of the approximate chi-squared probability distribution for all previous M observations of the model function.

Compared with other approaches, we show that the proposed Bayesian target-vector optimization (BTVO) scheme often requires significantly fewer iterations to reconstruct the desired model parameters. Another important advantage of the approach is that each GP offers a good non-linear model of the corresponding data channel. This enables, e.g., to quickly sample from the approximated posterior probability distribution of the model parameters and to accurately quantify parameter uncertainties.

The paper is organized as follows. In Section 2 we give a theoretical introduction into parameter reconstructions and into solving the corresponding least-squares problems. We review BO methods and their extension by Uhrenholt and Jensen. We then discuss the shortcomings for a large number of data channels K and introduce a mitigation strategy. We then discuss MCMC sampling for determining the uncertainties of the reconstructed parameters, and we describe

a way to drastically reduce the required number of model evaluations by training and evaluating surrogate models. In Section 3 we compare the performance of the proposed BTVO against a selection of established optimization methods. We consider three different model functions: a computationally expensive real-world optical metrology example, and two analytical model functions obtained from the NIST Standard Reference Database [20]. The two analytical model functions are additionally used to highlight the benefit of derivative information for the reconstruction performance. Finally, in Section 4 we employ one of the analytical model functions further to demonstrate the efficiency and accuracy of the surrogate model augmented MCMC method.

2 Theoretical background

Parameter reconstructions are often based on fitting the vectorial output of a parameterized model function $\mathbf{f}(\mathbf{p})$ to an experimental measurement $\mathbf{d} = (d_1, \dots, d_K)^T$, where $\mathbf{p} \in \mathcal{X} \subset \mathbb{R}^N$ and $\mathbf{f} : \mathcal{X} \rightarrow \mathbb{R}^K$. As usual, we assume that the model describes the measurement process sufficiently well, such that model errors can be neglected. Measurement noise is modelled by assuming that the i -th measurement value is equal to the model value for the true parameter \mathbf{p}_t plus some noise contribution,

$$d_i = f_i(\mathbf{p}_t) + \varepsilon_i.$$

Usually, the noise is modeled to be normally distributed with zero mean and variance η_i^2 , i.e., $\varepsilon_i \sim \mathcal{N}(0, \eta_i^2)$.

Finding a good estimate for \mathbf{p}_t can be considered an optimization task. We can obtain the maximum likelihood point estimate

$$\mathbf{p}_{\text{MLE}} = \arg \min_{\mathbf{p} \in \mathcal{X}} \chi^2(\mathbf{p})$$

by minimizing the sum of the squared residuals

$$\chi^2(\mathbf{p}) = \sum_{i=1}^K \frac{(f_i(\mathbf{p}) - d_i)^2}{\eta_i^2}. \quad (1)$$

Having determined \mathbf{p}_{MLE} , one is often also interested in the local probability distribution of the parameter values in order to determine confidence intervals of the reconstructed parameter values (c.f. Appendix A in the supplementary material).

In optical metrology applications, evaluating the model function \mathbf{f} typically involves running a numerical simulation, which can include the assembly of the discretized problem, numerical solution of differential equations, and postprocessing of the results. Calculating the result of the model function for a single set of parameters can therefore take a lot of computation time, depending on the complexity of the model and on numerical accuracy requirements.

2.1 Established approaches for parameter reconstruction

Minimizing Equation (1) can be done, e.g., using local methods such as the Gauß-Newton scheme or the Levenberg-Marquardt algorithm [17], or using global heuristic methods, for example particle swarm optimization [21, 22] or differential evolution [23, 24], or by maximizing the appropriate likelihood function using Markov chain Monte Carlo (MCMC) sampling methods [25].

An estimate for the confidence intervals can be obtained, e.g., by exploiting information about the derivatives of the model function with respect to each parameter at the point estimate \mathbf{p}_{MLE} , as is for example available after minimizing Equation (1) using least-squares methods [26, 27, 28], or by applying MCMC sampling methods to the appropriate likelihood function [29]. The latter has the advantage that one can obtain accurate uncertainties in terms of 16 %, 50 % (i.e., the median), and 84 % quantiles of the actual model parameter distributions, as well as determine nonlinear correlations between model parameters. Methods that exploit local derivative information usually only yield approximate Gaussian parameter uncertainties in terms of 1σ intervals, and are only capable of establishing linear correlations between model parameters. We denote these Gaussian parameter uncertainties as ϵ_{MLE} .

Using these established approaches to perform parameter reconstructions can be a computationally costly endeavour. Standard least-squares algorithms reconstruct the first minimum that they reach, which depends on the initial guess fed into the method. In more complex energy landscapes this can be a local minimum rather than the point estimate \mathbf{p}_{MLE} one seeks, a problem which can be alleviated, e.g., by using a multi-start approach. This does however not guarantee that \mathbf{p}_{MLE} is found. Particle swarm optimization and differential evolution on the other hand are not designed to be efficient in the sense that they obtain the point estimate in as few evaluations of the model function as possible, and MCMC sampling methods even *rely* on the fact that they evaluate the model function very often, since the quality of the reconstruction increases with the number of samples drawn [30]. This can present an issue from a resource standpoint, and necessitates more resource efficient optimization methods.

2.2 Bayesian optimization approaches for parameter reconstruction

Bayesian optimization (BO) methods [7, 8] are sequential optimization methods and are known for being very efficient at performing global optimizations of expensive black-box functions [31, 10]. To this end BO methods train a stochastic *surrogate model* – most often a Gaussian process (GP) [9] – in an iterative fashion, using all previous observations of the model function. This surrogate model is usually much quicker to eval-

uate than the model function itself. The predictions made by the surrogate model are then used by an acquisition function to determine a parameter \mathbf{p}_{m+1} which is beneficial to sample the model function with next. The exact meaning of "beneficial" in this context depends very much on the strategy pursued by the acquisition function, as well as the optimization goal.

In Subsection 2.2.1 we shortly introduce GPs and Gaussian process regression and describe in Subsection 2.2.2 how it is used in "conventional" BO for minimizing $\chi^2(\mathbf{p})$. In Subsection 2.2.3 we will discuss the BTVO approach proposed by Uhrenholt and Jensen [12], which minimizes Equation (1) by considering the individual contributions of the components of $\mathbf{f}(\mathbf{p})$.

2.2.1 Gaussian process regression

A GP is specified by a mean function $\mu : \mathcal{X} \rightarrow \mathbb{R}$ and a covariance kernel function $k : \mathcal{X} \times \mathcal{X} \rightarrow \mathbb{R}$. A usual choice for mean and covariance kernel function, which is also considered in the following, are a constant mean function and the Matérn 5/2 covariance function [32]

$$\begin{aligned} \mu(\mathbf{p}) &= \mu_0, \\ k(\mathbf{p}, \mathbf{p}') &= \sigma_0^2 \left(1 + \sqrt{5}r + \frac{5}{3}r^2 \right) \exp(-\sqrt{5}r), \\ \text{where } r &= \sqrt{\sum_{i=1}^N \frac{(p_i - p'_i)^2}{l_i^2}}. \end{aligned} \quad (2)$$

Up to some maximum number of observations M_{hyper} the hyperparameters $\mu_0, \sigma_0, l_1, \dots, l_N$ are chosen to maximize the likelihood of the observations [33, 34]. Afterwards, only μ_0, σ_0 are optimized and the length scales l_1, \dots, l_N , which enter the covariance function in a non-trivial way, are kept constant. A GP trained on function evaluations $\mathbf{Y} = [f(\mathbf{p}_1), \dots, f(\mathbf{p}_M)]^T$ allows to make predictions for any parameter vector \mathbf{p}^* in the form of a normally distributed random variable $\hat{f}(\mathbf{p}^*) \sim \mathcal{N}(\bar{y}(\mathbf{p}^*), \sigma^2(\mathbf{p}^*))$ with mean and variance

$$\bar{y}(\mathbf{p}^*) = \mu_0 + \mathbf{k}^T(\mathbf{p}^*) \mathbf{K}^{-1} [\mathbf{Y} - \mu_0 \mathbf{1}] \quad (3)$$

$$\sigma^2(\mathbf{p}^*) = \sigma_0^2 - \mathbf{k}^T(\mathbf{p}^*) \mathbf{K}^{-1} \mathbf{k}(\mathbf{p}^*), \quad (4)$$

where $\mathbf{k}(\mathbf{p}^*) = [k(\mathbf{p}^*, \mathbf{p}_1), \dots, k(\mathbf{p}^*, \mathbf{p}_M)]^T$ and $(\mathbf{K})_{ij} = k(\mathbf{p}_i, \mathbf{p}_j)$.

For better numerical stability, the positive semidefinite covariance matrix \mathbf{K} is not inverted directly. Instead, one can compute its Cholesky decomposition $\mathbf{K} = \mathbf{L}_K \mathbf{L}_K^T$ into a lower and upper triangular matrix in $\mathcal{O}(M^3)$ steps for $M \leq M_{\text{hyper}}$. For constant length scales (i.e., $M > M_{\text{hyper}}$) an update of the decomposition only requires $\mathcal{O}(M^2)$ steps [34]. Afterwards, one solves

$$\mathbf{L}_K \mathbf{L}_K^T \boldsymbol{\alpha} = \mathbf{Y} - \mu_0 \mathbf{1} \quad (5)$$

for $\boldsymbol{\alpha}$ by forward and backward substitution and

$$\mathbf{L}_K \boldsymbol{\beta}(\mathbf{p}^*) = \mathbf{k}(\mathbf{p}^*) \quad (6)$$

for $\boldsymbol{\beta}(\mathbf{p}^*)$ by forward substitution both in $\mathcal{O}(M^2)$ steps. With the auxiliary vectors $\boldsymbol{\alpha}$ and $\boldsymbol{\beta}$, Equations (3)

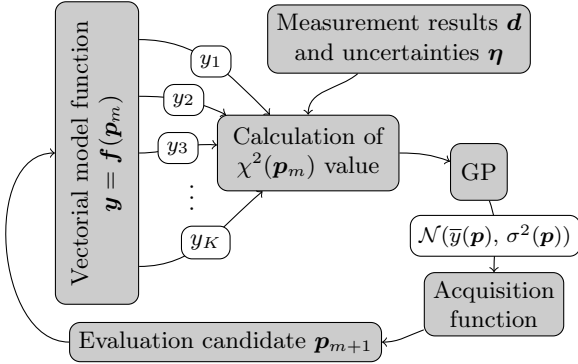


Figure 1: Schematic of a least-squares fit using the conventional Bayesian optimization method. The multiple outputs of the actual model are used to calculate the value of $\chi^2(\mathbf{p}_m)$ in Equation (1) for some parameter \mathbf{p}_m , which is then used to train the surrogate model (in this case a Gaussian process, GP). This surrogate predicts a normal distribution for each point in the parameter space, which is used by the acquisition function. The acquisition function determines a candidate parameter \mathbf{p}_{m+1} which is used to evaluate the actual model function again.

and (4) can be evaluated as $\bar{y}(\mathbf{p}^*) = \mu_0 + \mathbf{k}(\mathbf{p}^*)^T \boldsymbol{\alpha}$ and $\sigma^2(\mathbf{p}^*) = \sigma_0^2 - \boldsymbol{\beta}^T \boldsymbol{\beta}$ in only $\mathcal{O}(M)$ steps. For the computation of the next sampling point, one requires predictions for many points \mathbf{p}^* . Hence, solving Equation (6) for A different values of \mathbf{p}^* (typically $A \gtrsim 1000$) requires a large fraction of the computation time.

Training of GPs can be easily extended to exploit derivative information if available [34]. While this enlarges the number of data points and the size of the covariance matrix accordingly, all the above considerations are equally valid.

2.2.2 Bayesian optimization

First, we consider the conventional BO method in order to minimize the scalar function $\chi^2(\mathbf{p})$ defined in Equation (1). At each iteration m , the BO approach employs the predictions made by the trained GP in order to determine the next sampling point \mathbf{p}_{m+1} . This point is selected according to some infill criterion at the maximum of an acquisition function $\alpha(\mathbf{p})$ [7, 8]. A usual choice is the expected improvement (EI) with respect to the lowest known function value $\chi^2_{\min} = \min\{\chi^2(\mathbf{p}_1), \dots, \chi^2(\mathbf{p}_M)\}$.

The corresponding acquisition function is defined as

$$\alpha_{\text{EI}}(\mathbf{p}) = \mathbb{E} \left[\min(0, \chi^2_{\min} - \hat{f}(\mathbf{p})) \right], \quad (7)$$

where $\hat{f}(\mathbf{p})$ is a Gaussian random variable with mean $\bar{y}(\mathbf{p})$ and variance $\sigma^2(\mathbf{p})$ given in Equations (3) and (4). Another infill criterion is the lower confidence bound (LCB) with acquisition function

$$\alpha_{\text{LCB}}(\mathbf{p}) = \kappa \sigma^2(\mathbf{p}) - \bar{y}(\mathbf{p}), \quad (8)$$

where κ is a scaling factor.

2.2.3 Bayesian target-vector optimization

Directly minimizing the squared error function Equation (1) using BO (c.f. Figure 1) has some important drawbacks. First, it ignores the knowledge of the function values $f_1(\mathbf{p}), \dots, f_K(\mathbf{p})$ that contribute to the value of $\chi^2(\mathbf{p})$ in Equation (1). This information loss leads to a significantly slower convergence. The second issue stems from the fact that a GP can only be used to predict normal distributions, i.e., Equations (3) and (4). The predictions of a GP that has been conditioned on observations of Equation (1) are necessarily incorrect, since $\chi^2(\mathbf{p})$ does not follow a normal distribution, but rather a chi-squared distribution. This problem becomes especially pronounced when the GP predicts small mean values and large variances, as this may lead the acquisition function into exploring regions where the predictions suggest an improvement to negative χ^2 mean values. This clearly conflicts with χ^2 being larger than, or equal to, zero. To address the issues, we follow the approach proposed by Uhrenholt and Jensen [12], in which each of the K components of $\mathbf{f}(\mathbf{p})$ is modeled by a GP.

Using K independent GPs for making a regression on K channels increases the computational effort to $\mathcal{O}(K \cdot M^3)$ steps for computing K Cholesky decompositions. For $M > M_{\text{hyper}}$ observations we keep the length scales constant and the computational effort increases to $\mathcal{O}(A \cdot K \cdot M^2)$ steps for making A different prediction in order to maximize the acquisition function. For metrology applications with often more than 100 channels, the corresponding computation times render the approach impractical. Therefore, in contrast to the approach of Uhrenholt and Jensen, we propose to model the GPs using the same covariance kernel function and only allow for different hyperparameters $\mu_0^{(i)}$ and $\sigma_0^{(i)}$ for each channel $i = 1, \dots, K$. Hence, the Cholesky decomposition has to be computed only once and can be used for all channels as well as for the solution of Equation (6). Only Equation (5) has to be solved for all K channels since it depends on the acquired function values \mathbf{Y} in each channel. However, the equation has to be solved only once to make an arbitrary number A of predictions for different parameter vectors \mathbf{p}^* . Since A is usually much larger than K , the computational overhead of $\mathcal{O}(K \cdot M^2)$ steps for solving Equation (5) for each channel turns out to be acceptable in comparison to solving Equation (6) repeatedly in $\mathcal{O}(A \cdot M^2)$ steps.

The K GPs each provide predictions in form of a normally distributed random variable $\hat{f}_i(\mathbf{p}) \sim \mathcal{N}(\bar{y}_i(\mathbf{p}), \sigma_i^2(\mathbf{p}))$, for $i = 1, \dots, K$, such that the prediction of $\chi^2(\mathbf{p})$ defined in Equation (1) is a random variable

$$\hat{\chi}^2(\mathbf{p}) = \sum_{i=1}^K \frac{(\hat{f}_i(\mathbf{p}) - d_i)^2}{\eta_i^2}. \quad (9)$$

which follows a *generalized* chi-squared distribution. We note, that modelling $\hat{f}_1(\mathbf{p}), \dots, \hat{f}_K(\mathbf{p})$ as independent random variables neglects correlations between the channels. However, modelling these correlations

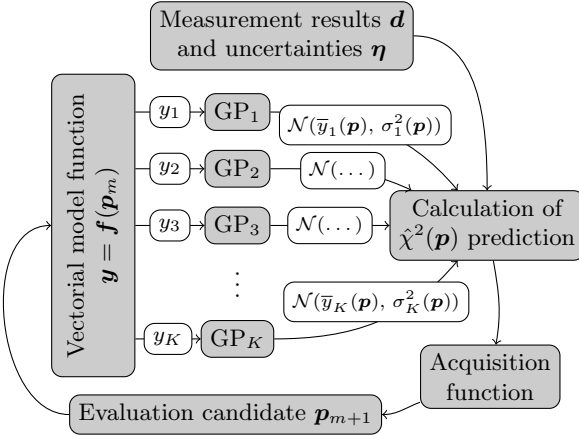


Figure 2: Schematic of a least-squares fit using the Bayesian target-vector optimization method. The K outputs of the actual model function are used to train K surrogate models (in this case K Gaussian processes), each of which predicts a normal distribution for each point in the parameter space, which are used to calculate a predicted $\hat{\chi}^2$ distribution. This predicted distribution is then used by the acquisition function, which in turn determines a candidate parameter \mathbf{p}_{m+1} , which is used to evaluate the actual model function again.

by training of a joint GP for all channels is computationally very expensive since the covariance matrix of the joint GP has $K^2 \cdot M^2$ instead of just M^2 entries.

The values of the probability distribution function (PDF) and cumulative distribution function (CDF) of $\hat{\chi}^2(\mathbf{p})$ are in general expensive to calculate [35, 36]. In order to be able to efficiently compute the distribution, Uhrenholt and Jensen resort to approximating the generalized chi-squared probability distribution by a *non-central* chi-squared distribution of the renormalized random variable $\hat{\chi}^2_{\text{ren}}(\mathbf{p}) \approx \hat{\chi}^2(\mathbf{p})/\gamma^2(\mathbf{p})$ with K degrees of freedom, average normalized variance

$$\gamma^2(\mathbf{p}) = \frac{1}{K} \sum_{i=1}^K \frac{\sigma_i^2(\mathbf{p})}{\eta_i^2}, \quad (10)$$

and non-centrality parameter

$$\lambda(\mathbf{p}) = \frac{1}{\gamma^2(\mathbf{p})} \sum_{i=1}^K \frac{(\bar{y}_i(\mathbf{p}) - d_i)^2}{\eta_i^2}. \quad (11)$$

This approximation is now followed by a second approximation, in which the non-central chi-squared distribution is approximated by a parameterized normal distribution. This makes it possible to evaluate the LCB infill criterion of the multi-output GP prediction Equation (9) with good efficiency and accuracy [12]. In a previous publication we successfully applied the described method to a parameter reconstruction problem for a relatively small number of data channels K [37]. Figure 2 shows a schematic of the BTVO being used to minimize Equation (1).

In order to demonstrate the issues that arise for a large number of data channels for this series of approximations, we consider a Wilson-Hilferty approximation

of the non-central chi-squared distribution, according to which the random variable

$$\hat{z}(\mathbf{p}) = \left(\frac{\gamma^{-2}(\mathbf{p}) \hat{\chi}^2(\mathbf{p})}{K + \lambda(\mathbf{p})} \right)^{1/3}$$

approximately follows a normal distribution [38] with mean $\bar{z}(\mathbf{p}) = 1 - 2/9\nu(\mathbf{p})$ and variance $\sigma_z^2(\mathbf{p}) = 2/9\nu(\mathbf{p})$, where $\nu(\mathbf{p}) = (K + \lambda(\mathbf{p}))^2 / K + 2\lambda(\mathbf{p})$. We consider the limit of $K \rightarrow \infty$ while keeping the non-centrality $\lambda(\mathbf{p})/K$ per channel constant. This is a good approximation for the case that the density of data channels in an experiment, e.g., the density of a measured spectrum, is increased. When increasing K , we observe that $\sigma_z^2(\mathbf{p}) \rightarrow 0$, which means that the PDF approaches a δ -distribution and the CDF a step function. Since $\bar{z}(\mathbf{p}) \rightarrow 1$, the maximum of the PDF approaches

$$\begin{aligned} \chi^2_{\text{mode}}(\mathbf{p}) &\rightarrow \gamma^2(\mathbf{p})(K + \lambda(\mathbf{p})) \\ &= \sum_{i=1}^K \frac{(\bar{y}_i(\mathbf{p}) - d_i)^2 + \sigma_i^2(\mathbf{p})}{\eta_i^2}. \end{aligned} \quad (12)$$

Let \mathbf{p}_{\min} be the parameter with the minimal observed value of χ^2 . Moving away from \mathbf{p}_{\min} to regions with fewer training samples, $\bar{y}_i(\mathbf{p})$ approaches the mean value of the corresponding GP, $\mu_0^{(i)}$, which has generally a larger deviation from the measurement d_i . Moreover the GP uncertainty increases. Hence, using this approximated probability function for large K the probability density of seeing χ^2 values smaller or close to $\chi^2(\mathbf{p}_{\min})$ quickly approaches zero for points not close to \mathbf{p}_{\min} . Consequently, the employed infill criterion can only select points close to \mathbf{p}_{\min} . In contrast to conventional BO, this leads to a very localized optimization behavior with possibly slow convergence and no exploration of regions with fewer training data. The selection of sample candidates that are too close to previously sampled positions also has a negative impact on the numerical stability of the scheme, as it leads to an ill-conditioned covariance matrix \mathbf{K} . Therefore, the optimization is terminated if the infill criterion is only able to select samples that are within a distance of 1×10^{-3} length scales to previously sampled positions.

This undesired behaviour of the approximate probability distribution for large K is a consequence of modelling all channels by independent random variables. For parameter reconstruction problems we know, however, that there exist parameter values for which *all* K residuals are small at the same time – an event that is expected to be almost impossible if K is large. Moreover, channels that belong to similar experimental conditions (e.g., similar angles and wavelengths in scatterometry experiments) show a similar dependence on the parameters \mathbf{p} and are thus positively correlated. If sum rules apply to the measurement process (e.g., energy or momentum conservation) also negative correlations between the channels can be observed. As described above, neglecting these \mathbf{p} -dependent correlations is done for performance reasons.

To mitigate these issues, we propose to replace the number of degrees of freedom K in the parameterization of the approximated probability distribution by

an *effective* number of degrees of freedom \tilde{K} , such that the approximate probability distribution better matches *all* M previous observations \mathbf{Y} of the model function. To this end, we take the sum over all χ_m^2 values, $\chi_{\text{all}}^2 = \sum_{m=1}^M \chi_m^2$, find the corresponding approximate marginal likelihood distribution, and then maximize the likelihood of the observed χ_{all}^2 value with respect to the effective degrees of freedom to obtain the maximum-likelihood estimate K_{MLE} . The acquisition function is then evaluated based on a non-central chi-squared distribution with $\tilde{K} = K_{\text{MLE}}$ effective degrees of freedom and non-centrality defined in Equation (11). The derivation of \tilde{K} is detailed in Appendix C in the supplementary material. We find that this yields an effective way to regain the exploratory nature of the BO method also for the BTVO with a large number of data channels K .

2.3 Markov chain Monte Carlo for accurate parameter uncertainties

Good estimates for the uncertainties of the reconstructed model parameters can be determined by using Markov chain Monte Carlo (MCMC) sampling methods [30, 39, 40]. To calculate them, MCMC draws samples from the likelihood function $\mathcal{L}(\mathbf{p})$ or the posterior probability $\mathcal{P}(\mathbf{p})$ (c.f. Appendix A in the supplementary material) of the model function $\mathbf{f}(\mathbf{p})$ at different positions in the parameter space. These samples are then used to construct an equilibrium distribution that resembles the sampled probability distribution. This equilibrium distribution then allows to infer the desired model parameter uncertainties in terms of the 16 %, 50 %, and 84 % quantiles of the model parameter distribution. MCMC can further expose non-linear correlations between model parameters, and it allows to fit a non-trivial error model to the observed data [41]. This makes MCMC a valuable tool for parameter reconstructions in general, not just in the field of optical metrology.

In practice, often tens of thousands of samples have to be drawn from the model function to construct a stable equilibrium distribution. For computationally expensive model evaluations, this can require very large computational resources.

2.3.1 Markov chain Monte Carlo on a Gaussian process surrogate

To lessen the resource impact of MCMC sampling, it can be favorable to use a trained and quick-to-evaluate surrogate model of the actual model function to construct the equilibrium distribution Markov chain. Recently, MCMC using surrogate models based on a polynomial chaos expansion [42] as well as invertible neural networks [43] were proposed and showed to be converging to the “exact” results, where “exact” in this context means that MCMC was performed on the model function directly.

We propose to instead utilize the multi-output GP surrogate model that was trained during a parameter

reconstruction with the BTVO scheme. It is used to calculate the predicted likelihood function $\hat{\mathcal{L}}(\mathbf{p})$ of the Gaussian prediction $\hat{\mathbf{f}}(\mathbf{p})$ of the model function, which is then used to generate the equilibrium distribution. We have to assert that the surrogate model is an accurate representation of the model function in the region of interest, which is often located around the acquired MLE point. Because the surrogate model was created during a parameter reconstruction, this region is often only explored reasonably well in the direction from which the MLE was found. To reduce the uncertainty of the surrogate model in the rest of the region of interest, we enter a refinement stage in which we train the model with more parameter samples close to the MLE point \mathbf{p}_{MLE} . To this end, we draw S random samples $\mathbf{p}_1, \dots, \mathbf{p}_S$ from the multivariate normal distribution $\mathcal{N}(\mathbf{p}_{\text{MLE}}, \text{Cov}(\mathbf{p}_{\text{MLE}}))$ defined by the parameter covariance matrix $\text{Cov}(\mathbf{p}_{\text{MLE}})$ at the MLE point (c.f. Appendix B in the supplementary material) and evaluate the forward model at the point with maximum mean uncertainty of the surrogate models of all channels, i.e.,

$$\mathbf{p}_{\text{max}} = \arg \max_{\mathbf{p} \in \{\mathbf{p}_1, \dots, \mathbf{p}_S\}} \frac{1}{K} \sum_{k=1}^K \sigma_k(\mathbf{p}).$$

We stop the additional sampling of the forward model when the maximum mean uncertainty is below some threshold σ_{min} .

3 Benchmarks

In order to assess the performance of the proposed BTVO scheme, we applied it to three parameter reconstruction problems: an experimental dataset, where the model function is a finite element simulation, and two synthetic datasets with analytic model functions.

The experimental dataset has been measured during a Grazing Incidence X-Ray Fluorescence (GIXRF) experiment at the synchrotron radiation source BESSY in Berlin [44]. The analytic datasets were obtained from the NIST Standard Reference Database [20] for non-linear regression problems. To show resilience of the reconstruction algorithm, we chose two datasets that differ with respect to the number of free parameters and data points: the MGH17 dataset [45] contains five free parameters and 33 data points, while the Gauss3 dataset [46] contains eight free parameters and 250 data points. The Gauss3 dataset is of particular interest, as it is comparable to problems from optical metrology in terms of free parameters and data points. Because of their analytical nature, derivatives with respect to all free parameters are easily calculated.

The proposed BTVO method was compared in a benchmark type analysis, where its reconstruction performance was compared to that of other optimization schemes. Here, Levenberg-Marquardt (LM) [1, 2, 47] (also c.f. Appendix B in the supplementary material, for the benchmarks we employed the `scipy.optimize.least_squares` [48]), BO as

detailed in Section 2.2.2, the limited memory Broyden–Fletcher–Goldfarb–Shanno algorithm with box constraints (L-BFGS-B) [49], as well as the Nelder–Mead (NM) downhill simplex algorithm [50] were used.

Of these methods, only BTVO and LM are methods that can solve least-squares problems natively by utilizing all data channels of the model function. BO, L-BFGS-B and NM are optimization methods that are usually used for the minimization or maximization of scalar functions. These methods therefore minimize (functions of) $\chi^2(\mathbf{p})$ as defined in Equation (1) directly. L-BFGS-B and NM both took the regular scalarized value $\chi^2(\mathbf{p})$ as model function, where L-BFGS-B explicitly profits from this as it works best on functions that are quadratic [51]. The surrogate model employed by BO assumes that the model function outputs are normally distributed. By taking the third root of a chi-squared distributed random variable it can be transformed into a more normally distributed random variable [52]. Therefore, BO minimized $(\chi^2)^{1/3}(\mathbf{p})$ instead of $\chi^2(\mathbf{p})$. Of the investigated methods only the Nelder–Mead algorithm can not take advantage of derivative information if provided.

For each reconstruction method and dataset, six consecutive optimizations were performed. From these results we calculated a mean and a standard deviation of the respective reconstruction result. The metric chosen to quantify the reconstruction performance of each method was the distance $d(\mathbf{p})$ of the reconstructed parameter to the MLE point \mathbf{p}_{MLE} , given in units of the Gaussian model parameter uncertainties ϵ_{MLE} , i.e.,

$$d(\mathbf{p}) = \sqrt{\sum_{i=1}^M \left(\frac{p_i - p_{\text{MLE},i}}{\epsilon_{\text{MLE},i}} \right)^2}. \quad (13)$$

We considered the reconstruction to be converged if parameter values with a distance $d < 0.1$ were found, i.e., the parameters deviated only by 10 % of the confidence interval.

To demonstrate the positive impact of using the effective degrees of freedom \tilde{K} to parameterize the predictive distribution in the BTVO scheme, we performed the same benchmarks as described above, but instead using the number of data channels K to parameterize the predictive distribution.

Afterwards, we assessed the efficiency of surrogate model augmented MCMC sampling by applying it to the MGH17 dataset, and compared the results to those of MCMC sampling applied to the exact likelihood function.

The reconstruction of the GIXRF problem was performed on a Dell PowerEdge R7525 Rack Server with 2x AMD EPYC 7542 32-core CPUs (yielding 128 usable threads) and 1 TB of RAM installed. The reconstructions of the two analytical problems were done on a workstation computer with a AMD Ryzen 7 3700X 8-core CPU and 32 GB of RAM.

3.1 The experimental dataset: Grazing Incidence X-Ray Fluorescence (GIXRF)

Grazing Incidence X-Ray Fluorescence (GIXRF) [53, 54] is an indirect optical measurement method that can be used to quantify samples both in terms of their geometry as well as in their material composition. To investigate a sample, it is illuminated using X-ray light. The incident radiation penetrates the sample to a certain depth that depends on the incoming angle θ (c.f. Figure 3). A large fraction of the incoming radiation is reflected. The reflected radiation interferes with the incident radiation and leads to the so-called X-ray standing wave (XSW) field. A small fraction of the incident radiation is absorbed by the sample and promptly given off again in the form of fluorescent light. Regions with constructive interference contribute more strongly to the fluorescence signal. As penetration depth and XSW depend strongly on the incidence angle θ , so does also the fluorescence spectrum, which is recorded by a calibrated silicon drift detector (SDD) oriented perpendicular to the incident radiation beam \mathbf{k}_{in} [55]. To determine the geometrical (and experimental) parameters of the sample using a set of experimentally obtained fluorescence intensities, a parameterized forward model of the experimental measurement process was created. In this model, a simulation of the electromagnetic fields of the XSW is performed. The modified 2D Sherman equation is then used to determine the numerical fluorescence intensity for each angle of incidence found in the experimental dataset [54].

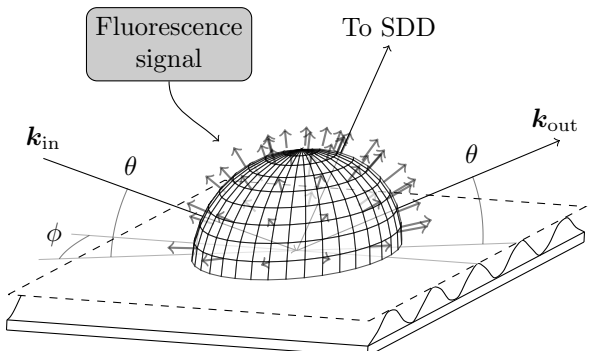


Figure 3: Illustration of the GIXRF measurement process. X-ray light with wave vector \mathbf{k}_{in} is used to illuminate the sample. A fraction of the incoming light is first absorbed by the sample and afterwards emitted as a fluorescence spectrum. This can be detected by a silicon drift detector (SDD) which is oriented perpendicular to the incoming radiation, \mathbf{k}_{in} .

The experimental dataset obtained for X-ray light with an energy of 520 eV contains 208 discrete datapoints shown in Figure 5. Note that the measurement uncertainties are approximately two orders of magnitude smaller than the measurement signal. The GIXRF reconstruction problem contains ten free parameters. Seven parameters describe the shape of the sample (c.f. Figure 4), one parameter scales the cal-

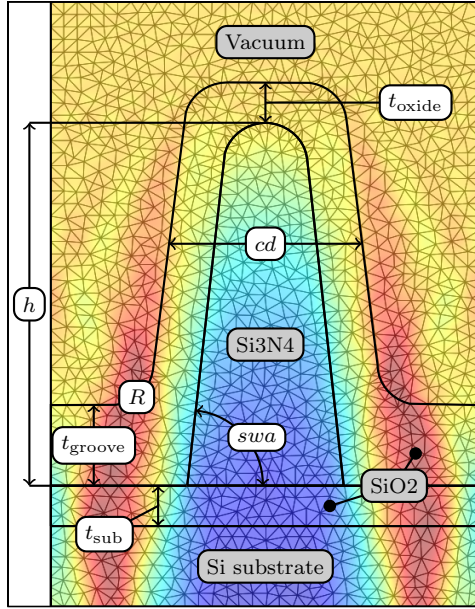


Figure 4: A unit cell of the GIXRF forward model with periodic boundary conditions in horizontal direction and perfectly absorbing boundary conditions in vertical direction. The geometric parameters are shown in white, the different materials are shown in grey. Additionally displayed are an exemplary finite element discretization and a simulated electric field intensity in pseudocolors.

culated intensities to the experimental intensities, and two free parameters have been introduced to account for uncertainties in the angles of incidence θ and ϕ (c.f. Figure 3). A listing of the employed parameter optimization intervals is given in Table 1. The densities of Si_3N_4 and SiO_2 , $\rho_{\text{Si}_3\text{N}_4} = 2.836 \text{ g cm}^{-3}$ and $\rho_{\text{SiO}_2} = 2.093 \text{ g cm}^{-3}$, were obtained by means of a separate X-ray reflectometry experiment [54]. The parameterized forward model was created using the finite-element Maxwell solver JCMsuite.

3.1.1 Reconstruction results

Figure 6 shows the performance of the employed optimization methods at reconstructing the geometrical and experimental model parameters for the GIXRF dataset. The benchmark's mean is depicted as a solid line, while its standard deviation is shown as a shaded band around the mean. Figure 6 (a) shows the progress of the reconstruction in terms of calls to the model function, while Figure 6 (b) shows it in terms of the actual wall time. This differentiation highlights the slight computational overhead of the Bayesian methods, where we are focusing on comparing the BTVO and LM in particular. BTVO required approximately 40 iterations to cross the (arbitrarily chosen) $d = 1$ threshold, while LM required approximately 88 iterations, an increase of 120 %. If we consider the wall time, BTVO required approximately 32 min to cross the $d = 1$ threshold and LM required approximately 68 min, which is a slightly smaller increase of 110 %. For model

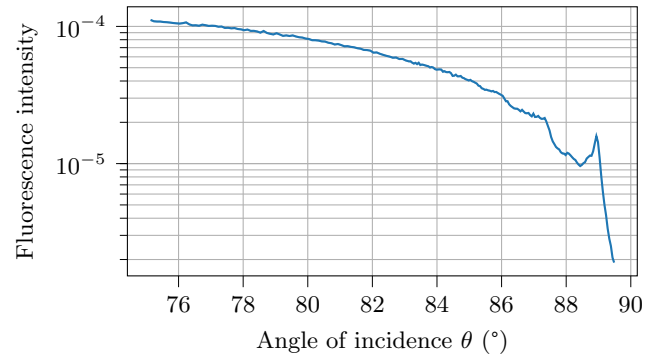


Figure 5: The experimentally recorded fluorescence intensity signal stemming from the Nitrogen in the core of the sample. The signal consists of 208 data points between angles of $\theta = 75.13^\circ$ and $\theta = 89.48^\circ$.

functions with very short computation times, such as models described by analytic functions, BTVO may not necessarily be advantageous.

Of the employed reconstruction algorithms, only the proposed BTVO and LM managed to reconstruct the parameters to an average of less than one standard deviation of the MLE. The BTVO reached an average distance of $d \approx 0.13$, while LM reached an average distance of $d \approx 0.58$. The remaining schemes did not manage to utilize the provided optimization budget to reconstruct parameters within 10 standard deviations of the MLE.

The reconstructed parameters and associated Gaussian uncertainties $p_{\text{MLE}} \pm \epsilon_{\text{MLE}}$ due to the BTVO are found in Table 1. The values were rounded to the first significant digit of the reconstructed uncertainties. Explanations regarding to the meaning of the parameters can be found in the table caption of Table 1, as well as in Figures 3 and 4.

The X-ray light energy of 520 eV is sufficient to obtain a fluorescence signal from the Nitrogen within the core of the sample. Nevertheless, also the different oxide layer thicknesses t_{oxide} , t_{groove} , and t_{sub} could be reconstructed with small uncertainty, which is in agreement with the observation made by Soltwisch et al. [44].

3.2 Analytical datasets: MGH17 and Gauss3

Additionally, two analytical datasets were investigated. Here, the MGH17 [45] and Gauss3 [46] datasets were chosen. Both were obtained from the NIST Standard Reference Database [20]. The target values within the datasets were created using the respective model function, where a normally distributed error was added to each data point. Since the model functions are analytical in nature, derivatives are easily calculated. The model function used to fit the 33 datapoints of the MGH17 dataset is

$$f(x, \beta) = \beta_1 + \beta_2 e^{-x \cdot \beta_4} + \beta_3 e^{-x \cdot \beta_5} \quad (14)$$

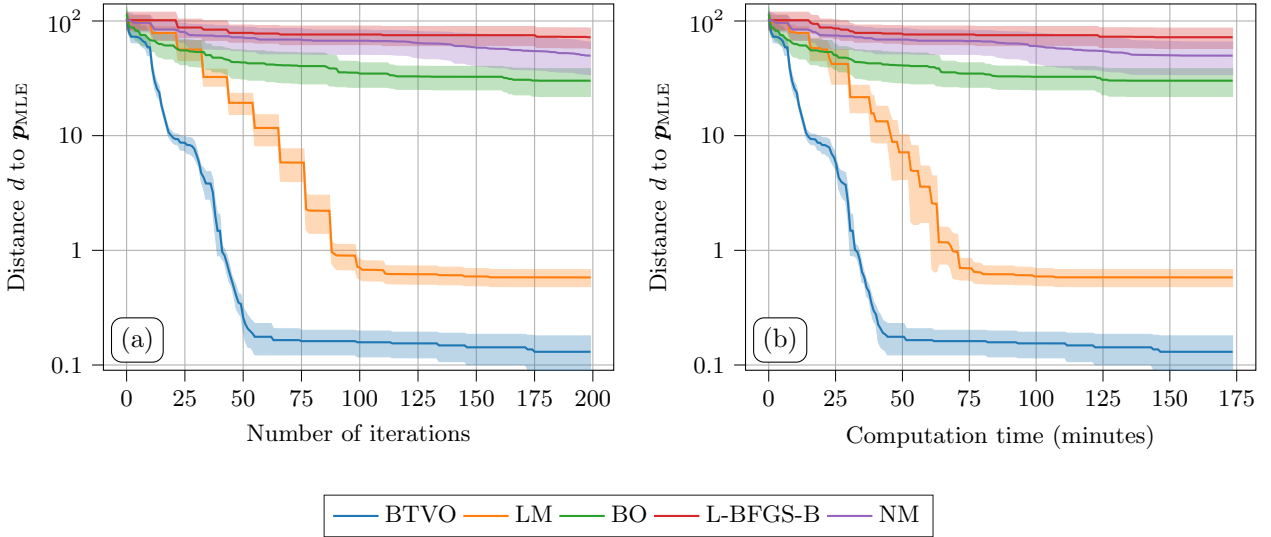


Figure 6: The progress of the parameter reconstruction of the GIXRF dataset for different reconstruction methods. The plots show the distance $d(\mathbf{p})$ to the MLE point \mathbf{p}_{MLE} , in units of the reconstructed Gaussian standard deviation ϵ_{MLE} (c.f. Equation (13)). Shown are the means (solid lines) and standard deviation (shaded bands) from six consecutive reconstruction runs. The x axis shows (a) the number of evaluations of the model function and (b) the time spent by each reconstruction method. None of the employed methods managed to reconstruct the parameters to an average distance of $d < 0.1$. Otherwise, the best reconstruction results are obtained by the BTVO scheme.

Parameter	Range	Reconstruction results
h (nm)	[85, 100]	89.5 ± 0.4
cd (nm)	[35, 55]	46.3 ± 0.2
swa ($^{\circ}$)	[75, 90]	83.7 ± 0.1
t_{oxide} (nm)	[1, 6]	2.21 ± 0.03
t_{groove} (nm)	[0.1, 10]	1.0 ± 0.3
t_{Sub} (nm)	[0.1, 10]	6.9 ± 0.9
R (nm)	[3, 10]	7.0 ± 0.8
s_N (1)	[0.5, 1.5]	0.727 ± 0.005
Δ_{θ} ($^{\circ}$)	[-0.15, 0.15]	-0.101 ± 0.003
Δ_{ϕ} ($^{\circ}$)	[-0.075, 0.075]	0.006 ± 0.009

Table 1: The fitting parameters, the corresponding ranges for the GIXRF model, as well as the results of the reconstruction due to the BTVO method, i.e., $\mathbf{p}_{\text{MLE}} \pm \epsilon_{\text{MLE}}$. The reconstruction results were rounded to the first significant digit of the reconstructed uncertainties. Listed are the height h , the critical dimension cd , the side wall angle swa , the thickness of the oxide layer on top of the structure t_{oxide} , the thickness of the oxide layer in the groove t_{groove} , the thickness of the substrate t_{sub} , the corner rounding radius R , a scaling parameter for the measured fluorescence s_N , as well as offset values for the angle of incidence θ and the azimuth angle ϕ , Δ_{θ} and Δ_{ϕ} respectively.

Parameter	Range	Certified value [45]
β_1	[0, 10]	0.374 ± 0.002
β_2	[0.1, 4]	1.9 ± 0.2
β_3	[-4, -0.1]	-1.5 ± 0.2
β_4	[0.005, 0.1]	0.0129 ± 0.0004
β_5	[0.005, 0.1]	0.0221 ± 0.0009

Table 2: List of parameters with certified fit results as taken from [45], as well as the employed parameter bounds for the MGH17 dataset. The certified results are rounded to the first significant digit of the given uncertainty.

Parameter	Range	Certified value [46]
β_1	[90, 110]	98.9 ± 0.5
β_2	[0.005, 0.05]	0.0109 ± 0.0001
β_3	[90, 110]	100.7 ± 0.8
β_4	[100, 120]	111.6 ± 0.4
β_5	[15, 30]	23.3 ± 0.4
β_6	[70, 80]	74 ± 1
β_7	[140, 150]	147.8 ± 0.4
β_8	[17, 22]	19.7 ± 0.4

Table 3: List of parameters with certified fit results as taken from [46], as well as the employed parameter bounds for the Gauss3 dataset. The certified results are rounded to the first significant digit of the given uncertainty.

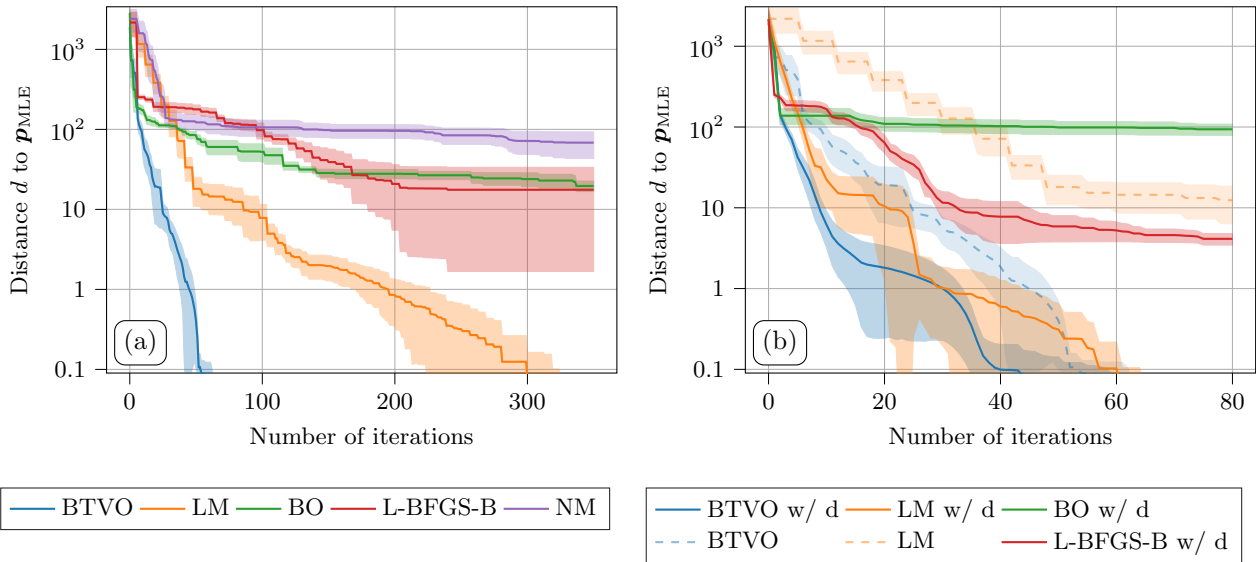


Figure 7: The progress of the parameter reconstruction of the MGH17 dataset without (a) and with (b) the use of derivative information. Note that figure (b) shows a truncated view, limited to 80 iterations. The plots show the distance $d(\mathbf{p})$ to the MLE point \mathbf{p}_{MLE} according to Equation (13). Shown are the means (solid and dashed lines) and standard deviation (shaded bands) from six consecutive reconstruction runs. The x axis shows the number of evaluations of the model function. Without the use of derivative information only BTVO and LM manage to reconstruct parameters that are within a distance $d < 0.1$. Taking accurate derivative information into consideration improves both the BTVO and especially the LM results. However, BTVO still outperforms LM.

and contains 5 free parameters (c.f. Table 2). The Gauss3 dataset consists of 250 discrete datapoints and is fit using the 8 parameter model function (c.f. Table 3)

$$f(x, \boldsymbol{\beta}) = \beta_1 e^{-\beta_2 \cdot x} + \beta_3 e^{-(x - \beta_4)^2 / \beta_5^2} + \beta_6 e^{-(x - \beta_7)^2 / \beta_8^2}. \quad (15)$$

3.2.1 MGH17 reconstruction results

The results for the optimization benchmarks of the MGH17 dataset are shown in Figure 7. Figure 7 (a) shows the results without the use of derivative information, while Figure 7 (b) shows the results which were obtained with accurate derivative information taken into consideration. For better visibility of the convergence behavior of BTVO and LM, we have truncated the number of iterations in Figure 7 (b) to 80. The other methods did not converge to $d < 0.1$ within an optimization budget of 350 iterations.

Without derivative information, only BTVO and LM were able to reconstruct the certified results (c.f. Table 2) within its standard deviations, as well as the uncertainty intervals. BTVO reached a value of $d < 0.1$ after approximately 54 iterations, while LM required 300 iterations. None of the remaining methods were able to get to within 10 standard deviations of \mathbf{p}_{MLE} before the optimization budget was exhausted.

When derivative information was taken into consideration the results for BTVO, LM, and L-BFGS-B improved. Both BTVO and LM were able to reach $d < 0.1$ (40 iterations for BTVO, 61 iterations for LM), and were ultimately also able to reconstruct the certi-

fied result within the provided optimization budget. We note that for this particular example BTVO *without* derivative information performs better than LM *with* derivative information.

The performance of the conventional BO worsened when including derivative information. We attribute this to the strong correlation of some of the parameters for this specific reconstruction problem (c.f. MCMC sampling). This is associated with large parameter regions with very similar values of χ^2 . Due to the expected improvement infill criterion, BO has troubles to converge in regions with very small gradients where it expects no relevant improvement. This problem might be exacerbated when derivative information are available.

NM is not able to make use of derivative information and was therefore not considered here.

3.2.2 Gauss3 reconstruction results

The results for the optimization benchmarks of the Gauss3 dataset are shown in Figure 8, where Figure 8 (a) depicts the results without the use of derivative information, while Figure 8 (b) shows the results that were obtained with accurate derivative information taken into consideration.

Without derivative information, BTVO again performed best and was able to reproduce the values of the certified result (c.f. Table 3) and its uncertainty intervals. In each of the six runs it was able to reconstruct parameters within less than 10 % of the MLE and reached $d < 0.1$ in approximately 38 iterations. LM was also able to achieve $d < 0.1$, and did so af-

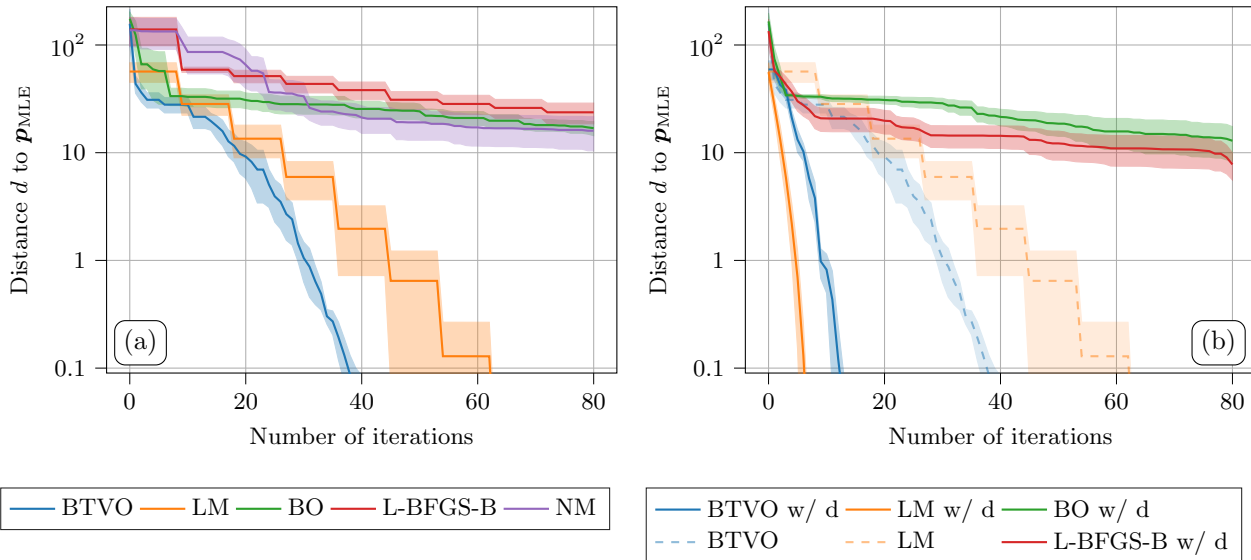


Figure 8: The progress of the parameter reconstruction of the Gauss3 dataset without (a) and with (b) the use of derivative information. The plots show the distance $d(\mathbf{p})$ to the MLE point \mathbf{p}_{MLE} according to Equation (13). Shown are the means (solid and dashed lines) and standard deviation (shaded bands) from six consecutive reconstruction runs. The x axis shows the number of evaluations of the model function. Both with and without derivative information, only BTVO and LM manage to reconstruct the parameters to within $d < 0.1$ in the provided optimization budget. Without derivative information BTVO performs better than LM, and with derivative information LM performs better than BTVO.

ter 63 iterations. The remaining three optimization schemes – BO, L-BFGS-B, and NM – were not able to get to within 10 standard deviations of \mathbf{p}_{MLE} .

Taking derivative information into consideration improved the reconstruction performance for all optimization schemes. L-BFGS-B was now also able to reconstruct the model parameters to within 10 standard deviations. Very drastic improvements were seen for both the proposed BTVO and LM schemes. BTVO now only required approximately 13 iterations to reconstruct model parameters within 10 % of the MLE, approximately a third of the iterations required without derivative information. The clearest benefactor of accurate derivative information however was LM, which was now able to reconstruct the model parameters to within 10 % in only 7 iterations. The performance of BO increased slightly, although not to the extent that we expected when providing accurate derivative information. We attribute this again to the behavior described in Section 3.2.1. However, as the model parameters of the Gauss3 problem are correlated not as strongly as those in the MGH17 problem, we can still observe a small improvement of the reconstruction result. NM is again not considered, as it cannot make use of derivatives.

3.3 BTVO without effective degrees of freedom

As detailed in Section 2.2.3, keeping the degrees of freedom fixed to the number of data channels K can lead to a very localized optimization behavior for the BTVO scheme. The associated selection of samples that are too close to previous sample positions leads to a ter-

mination of the optimization after a certain number of iterations. We have observed that model functions with a smaller number of data channels took longer to reach this point. The number of iterations taken by each model function are averages from six different runs. Here, the GIXRF reconstruction failed after an average of 14 iterations. The MGH17 reconstructions failed after an average of 73 iterations without, and 31 iterations with the use of derivatives. The Gauss3 reconstructions failed after an average of 14 iterations without, and only 4 iterations with the use of derivatives. During this small number of iterations, the BTVO scheme was only able to reconstruct parameters with $d < 1$ for the MGH17 problem.

4 Application of Markov chain Monte Carlo sampling

To demonstrate the capabilities of the surrogate model augmented MCMC sampling, we applied it to the analytic MGH17 dataset. The goal was to sample the predicted likelihood function $\hat{\mathcal{L}}(\mathbf{p})$, to extract the parameter uncertainties in terms of the 16 %, 50 % (or median), and 84 % quantiles of the parameter distributions, and to determine the correlations between the parameters of the model. Because the MGH17 dataset is based on an analytic function, we also applied MCMC to the exact likelihood function $\mathcal{L}(\mathbf{p})$ and compared the obtained results. To sample the respective likelihood functions we employed `emcee` [56].

The surrogate model was trained in two stages. In the parameter reconstruction stage the MLE was found within 63 iterations. Derivative information was not

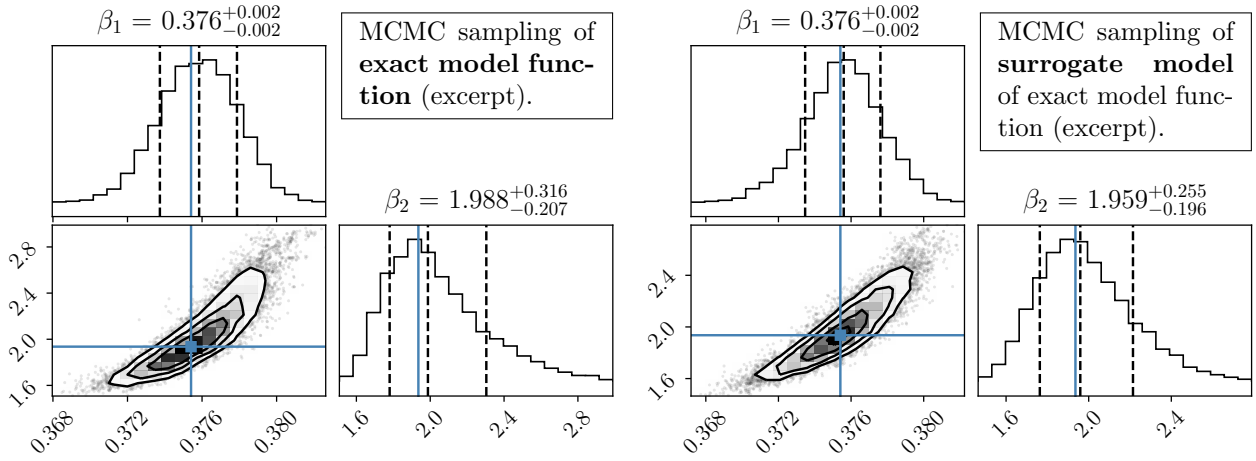


Figure 9: An excerpt of the results of MCMC sampling of the likelihood function of the MGH17 dataset, using the exact likelihood function (left) directly and using a trained multi-output surrogate model (right) to calculate a stochastic prediction of the likelihood function. Only the parameters β_1 and β_2 are shown. A direct comparison of the two results reveals that the surrogate model approach is capable of reproducing the model parameter distributions as well as revealing correlations between the individual model parameters, while using significantly fewer evaluations of the model function. The blue lines shown are the certified NIST results [45] (also c.f. Table 2). The remaining model parameters can be found in Figure S1 in the supplementary material.

used during the reconstruction. In the refinement stage, the uncertainty of the surrogate model in the region of interest around the MLE is reduced. At each refinement step, $S = 10 \cdot (N + 1)$ random samples were drawn and the one with the largest mean uncertainty was used to evaluate the model function and retrain the surrogate model. The refinement was stopped after the maximum mean uncertainty was below $\sigma_{\min} = 1 \times 10^{-4}$ times that of the global uncertainty in the surrogate model for five consecutive iterations, which was reached after an additional 41 iterations. The actual model function was thus evaluated 104 times.

Figure 9 shows an excerpt of the comparison of MCMC sampling of the exact likelihood function $\mathcal{L}(a, b, \mathbf{p})$ and the predicted likelihood function $\hat{\mathcal{L}}(a, b, \mathbf{p})$ around the MLE \mathbf{p}_{MLE} . In both instances, 32 MCMC walkers were used to draw 50 000 samples from the respective likelihood functions. The complete comparison for all parameters can be found in Figure S1 in the supplementary material.

The histograms at the top show the 16 %, 50 % (or median), and 84 % quantiles of the parameter distributions. Both the exact, as well as the surrogate aided MCMC samplings produced very similar histograms, both in terms of quantile values as well as in terms of the overall shape. The recovered values matched the certified results provided by the NIST within the reconstructed standard deviations.

The 2d scatter plots between the histograms highlight correlations between the model parameters. The displayed levels are – from inside to outside – the 0.5σ , 1σ , 1.5σ , 2σ regions. Again, both methods showed good agreement.

Finally, the method was used to assess the magni-

tude of the measurement uncertainties. To this end the basic error model

$$\tilde{\eta}_i = 2^{\eta_c} \cdot \eta_i$$

was fit to the data. The actual measurement uncertainties can be scaled up and down by fitting the value of the exponent η_c . Both MCMC sampling of the exact model and the surrogate model yield a value of η_c close to zero with an uncertainty of about ± 0.2 , c.f. Figure S1 in the supplementary material.

This demonstrates that qualitatively and quantitatively accurate results can be obtained with the surrogate model aided MCMC, which comes at a fraction of the cost of directly sampling the likelihood function (104 evaluations of the actual model function to train the surrogate model, instead of 50 000 evaluations to perform MCMC).

5 Conclusion

We have expanded a recently introduced Bayesian target-vector optimization (BTVO) scheme to be compatible with a much larger number of data channels K . We have done this by introducing a new parameterization, which adjusts the actual degrees of freedom to be an effective number of degrees of freedom, as well as by sharing the covariance function for the individual GPs among each other, such that only one matrix decomposition is necessary at each iteration of the optimization instead of one for each data channel.

We have applied the proposed BTVO to various parameter reconstruction tasks and have shown that the scheme regularly outperforms the established Levenberg-Marquardt algorithm at reconstructing model parameters during a least-squares fit, the

single exception being when derivative information has been directly exploited in one particular example.

We have further shown that the method can be extended to enable Markov chain Monte Carlo sampling of expensive model functions with largely reduced computational costs. This has been achieved by exploiting the multi-output surrogate model which was trained during the parameter reconstruction. By using an analytic model function we have demonstrated that the surrogate model approach is capable of generating results that are in good agreement with the exact results, while using only a fraction of the evaluations of the model function. In doing this, one is able to obtain model parameter uncertainties in terms of quantiles of the model parameter distributions, to determine non-linear correlations between parameters, and in principle also to fit a non-trivial error model to the data.

6 Supporting information

Supporting information can be found in the supplementary material.

7 Conflict of Interest

The authors declare no conflict of interest.

8 Acknowledgements

We acknowledge discussions with Victor Soltwisch, Martin Hammerschmidt, and Lin Zschiedrich, and we acknowledge Philipp Hönicke for assistance in recording the experimental data set. This project is funded by the German Federal Ministry of Education and Research (BMBF, project number 05M20ZAA, siMLOpt; project number 01IS20080A, SiM4diM; Forschungscampus MODAL, project number 05M20ZBM), by the German Federal Ministry for Economic Affairs and Energy (BMWi, project number 50WM2067, Optimal-QT), and by the European Union's Horizon 2020 research and innovation programme (EU H2020, grant number 101007319, AI-TWILIGHT).

References

- [1] K. Levenberg, *Q. Appl. Math.* **1944**, *2*, 2 164.
- [2] D. W. Marquardt, *J. Soc. Ind. Appl. Math.* **1963**, *11*, 2 431.
- [3] P. Deuflhard, *Newton methods for nonlinear problems: affine invariance and adaptive algorithms*, volume 35, Springer Science & Business Media, 2005.
- [4] E. Vogel, *Nat. Nanotechnol.* **2007**, *2* 25.
- [5] N. G. Orji, M. Badaroglu, B. M. Barnes, C. Beitia, B. D. Bunday, U. Celano, R. J. Kline, M. Neisser, Y. Obeng, A. Vladar, *Nat. Electron.* **2018**, *1* 532.
- [6] C. J. Raymond, M. E. Littau, A. Chuprin, S. Ward, *Proc. SPIE* **2004**, *5375* 564.
- [7] J. Močkus, In *Optimization techniques IFIP technical conference*. Springer, **1975** 400–404.
- [8] J. Močkus, *Bayesian approach to global optimization: theory and applications*, volume 37, Springer Science & Business Media, **2012**.
- [9] C. K. Williams, C. E. Rasmussen, *Gaussian processes for machine learning*, volume 2, MIT press Cambridge, MA, **2006**.
- [10] D. R. Jones, M. Schonlau, W. J. Welch, *J. Global Optim.* **1998**, *13*, 4 455.
- [11] K. Matsui, S. Kusakawa, K. Ando, K. Kutsukake, T. Ujihara, I. Takeuchi, *arXiv preprint arXiv:1911.03671* **2019**.
- [12] A. K. Uhrenholt, B. S. Jensen, In *The 22nd International Conference on Artificial Intelligence and Statistics*. PMLR, **2019** 2661–2670.
- [13] C. Huang, Y. Ren, E. K. McGuinness, M. D. Losego, R. P. Lively, V. R. Joseph, *Optimization and Engineering* **2021**, *22*, 4 2553.
- [14] B. M. Barnes, M.-A. Henn, *Proc. SPIE* **2020**, *11325* 113251E.
- [15] M. A. Alvarez, L. Rosasco, N. D. Lawrence, *arXiv preprint arXiv:1106.6251* **2011**.
- [16] H. Liu, J. Cai, Y.-S. Ong, *Knowl.-Based Syst.* **2018**, *144* 102.
- [17] M. Hammerschmidt, M. Weiser, X. G. Santiago, L. Zschiedrich, B. Bodermann, S. Burger, *Proc. SPIE* **2017**, *10330* 1033004.
- [18] V. Szwedowski-Rammert, J. Baumann, C. Schlesiger, U. Waldschläger, A. Gross, B. Kanngießer, I. Mantouvalou, *J. Anal. At. Spectrom.* **2019**, *34*, 5 922.
- [19] N. Kumar, P. Petrik, G. K. Ramanandan, O. El Gawhary, S. Roy, S. F. Pereira, W. M. Coene, H. P. Urbach, *Opt. Express* **2014**, *22*, 20 24678.
- [20] NIST, Standard Reference Database, **2003**, URL: <https://www.itl.nist.gov/div898/strd/index.html> (version: 2021-04-20).
- [21] M. Shokooh-Saremi, R. Magnusson, *Opt. Lett.* **2007**, *32*, 8 894.
- [22] S. M. Mirjalili, K. Abedi, S. Mirjalili, *Optik* **2013**, *124*, 23 5989.
- [23] E. Bor, M. Turduev, H. Kurt, *Sci. Rep.* **2016**, *6*, 1 1.

[24] M. G. Saber, A. Ahmed, R. H. Sagor, *Silicon* **2017**, *9*, 5 723.

[25] A. F. Herrero, M. Pflüger, J. Puls, F. Scholze, V. Soltwisch, *Opt. Express* **2021**, *29* 35580.

[26] M. H. Kutner, C. J. Nachtsheim, J. Neter, W. Li, *Applied Linear Statistical Models*, McGraw-Hill Irwin, 5 edition, **2005**.

[27] W. H. Press, S. A. Teukolsky, W. T. Vetterling, B. P. Flannery, *Numerical Recipes: The Art of Scientific Computing*, Cambridge University Press, 3 edition, **2007**.

[28] T. Strutz, *Data Fitting and Uncertainty: A Practical Introduction to Weighted Least Squares and Beyond*, Vieweg and Teubner, **2011**.

[29] M. Pflüger, R. J. Kline, A. F. Herrero, M. Hammerschmidt, V. Soltwisch, M. Krumrey, *J. Micro-Nanolithogr. MEMS MOEMS* **2020**, *19*, 1 014001.

[30] C. Andrieu, N. De Freitas, A. Doucet, M. I. Jordan, *Mach. Learn.* **2003**, *50*, 1 5.

[31] P.-I. Schneider, X. Garcia Santiago, V. Soltwisch, M. Hammerschmidt, S. Burger, C. Rockstuhl, *ACS Photonics* **2019**, *6*, 11 2726.

[32] E. Brochu, V. M. Cora, N. De Freitas, *arXiv preprint arXiv:1012.2599* **2010**.

[33] X. Garcia-Santiago, P.-I. Schneider, C. Rockstuhl, S. Burger, *J. Phys. Conf. Ser.* **2018**, *963*, 1 012003.

[34] X. Garcia-Santiago, S. Burger, C. Rockstuhl, P. I. Schneider, *J. Light. Technol.* **2021**, *39* 167.

[35] A. M. Mathai, S. B. Provost, *Quadratic forms in random variables: theory and applications*, Dekker, **1992**.

[36] A. A. Mohsenipour, Ph.D. thesis, University of Western Ontario, **2012**.

[37] M. Plock, S. Burger, P.-I. Schneider, *Proc. SPIE* **2021**, *11783* 117830J.

[38] S. Abdel-Aty, *Biometrika* **1954**, *41*, 3/4 538.

[39] C. Sammut, G. I. Webb, *Encyclopedia of machine learning*, Springer Science & Business Media, **2011**.

[40] J. Friedman, T. Hastie, R. Tibshirani, et al., *The elements of statistical learning*, volume 1, Springer series in statistics New York, **2001**.

[41] M.-A. Henn, H. Gross, F. Scholze, M. Wurm, C. Elster, M. Bär, *Opt. Express* **2012**, *20* 12771.

[42] N. Farchmin, M. Hammerschmidt, P.-I. Schneider, M. Wurm, B. Bodermann, M. Bär, S. Heidenreich, *J. Micro-Nanolithogr. MEMS MOEMS* **2020**, *19* 024001.

[43] A. Andrle, N. Farchmin, P. Hagemann, S. Heidenreich, V. Soltwisch, G. Steidl, In A. Elmoataz, J. Fadili, Y. Quéau, J. Rabin, L. Simon, editors, *Scale Space and Variational Methods in Computer Vision*. Springer International Publishing, Cham, ISBN 978-3-030-75549-2, **2021** 528–539.

[44] V. Soltwisch, P. Hönicke, Y. Kayser, J. Eilbracht, J. Probst, F. Scholze, B. Beckhoff, *Nanoscale* **2018**, *10* 6177.

[45] NIST Standard Reference Database, MGH17 dataset, **1972**, URL <https://www.itl.nist.gov/div898/strd/nls/data/mgh17.shtml>.

[46] NIST Standard Reference Database, Gauss3 dataset, **1996**, URL <https://www.itl.nist.gov/div898/strd/nls/data/gauss3.shtml>.

[47] R. Fletcher, A modified Marquardt subroutine for non-linear least squares, Technical Report AERE-R-6799, Atomic Energy Research Establishment, Harwell (England), **1971**.

[48] P. Virtanen, R. Gommers, T. E. Oliphant, M. Haberland, T. Reddy, D. Cournapeau, E. Burovski, P. Peterson, W. Weckesser, J. Bright, S. J. van der Walt, M. Brett, J. Wilson, K. J. Millman, N. Mayorov, A. R. J. Nelson, E. Jones, R. Kern, E. Larson, C. J. Carey, İ. Polat, Y. Feng, E. W. Moore, J. VanderPlas, D. Laxalde, J. Perktold, R. Cimrman, I. Henriksen, E. A. Quintero, C. R. Harris, A. M. Archibald, A. H. Ribeiro, F. Pedregosa, P. van Mulbregt, SciPy 1.0 Contributors, *Nat. Methods* **2020**, *17* 261.

[49] R. H. Byrd, P. Lu, J. Nocedal, C. Zhu, *SIAM J. Sci. Comp.* **1995**, *16*, 5 1190.

[50] J. A. Nelder, R. Mead, *Comput. J.* **1965**, *7*, 4 308.

[51] D. C. Liu, J. Nocedal, *Math. Program.* **1989**, *45*, 1 503.

[52] D. M. Hawkins, R. Wixley, *Am. Stat.* **1986**, *40*, 4 296.

[53] Y. Ménesguen, B. Boyer, H. Rotella, J. Lubeck, J. Weser, B. Beckhoff, D. Grötzsch, B. Kanngießer, A. Novikova, E. Nolot, M.-C. Lépy, *X-Ray Spectrom.* **2017**, *46*, 5 303.

[54] A. Andrle, P. Hönicke, G. Gwalt, P.-I. Schneider, Y. Kayser, F. Siewert, V. Soltwisch, *Nanomaterials* **2021**, *11* 1647.

[55] P. Hönicke, A. Andrle, Y. Kayser, K. V. Nikolaev, J. Probst, F. Scholze, V. Soltwisch, T. Weimann, B. Beckhoff, *Nanotechnology* **2020**, *31* 505709.

[56] D. Foreman-Mackey, D. W. Hogg, D. Lang, J. Goodman, *Publ. Astron. Soc. Pac.* **2013**, *125* 306.

[57] M. H. DeGroot, M. J. Schervish, *Probability and statistics*, Pearson, 4 edition, **2012**.

- [58] V. Soltwisch, A. Fernández Herrero, M. Pflüger, A. Haase, J. Probst, C. Laubis, M. Krumrey, F. Scholze, *J. Appl. Crystallogr.* **2017**, *50* 1524.
- [59] P.-I. Schneider, M. Hammerschmidt, L. Zschiedrich, S. Burger, *Proc. SPIE* **2019**, *10959* 1095911.
- [60] G. A. Seber, C. J. Wild, *Nonlinear regression*, John Wiley & Sons, Inc., Hoboken, New Jersey, **2003**.
- [61] M. Sankaran, *Biometrika* **1959**, *46*, 1/2 235.

Supplementary Material

A Parameter reconstruction using Bayesian inference

In this section we go into more detail on the probabilistic background of parameter reconstructions. Given some experimental measurement $\mathbf{d} = (d_1, \dots, d_K)^T$ and a parameterized vectorial model $\mathbf{f}(\mathbf{p})$ of that measurement with $\mathbf{p} \in \mathcal{X} \subset \mathbb{R}^N$ and $\mathbf{f} : \mathcal{X} \rightarrow \mathbb{R}^K$, a parameter reconstruction consist of finding model parameters \mathbf{p} such that $\mathbf{f}(\mathbf{p})$ best matches \mathbf{d} . For the true parameter vector \mathbf{p}_t the i -th model output is equal to the measurement result plus a noise contribution, i.e.

$$d_i = f_i(\mathbf{p}_t) + \epsilon_i.$$

We further assume no correlations between the measurements and no systematic errors. The noise is modeled to be normally distributed with zero mean and variance η_i^2 , i.e. $\epsilon_i \sim \mathcal{N}(0, \eta_i^2)$.

To obtain an estimate for the true parameter in the Bayesian sense one defines a probability density function (PDF) for the model parameters and maximizes this density with respect to all parameters of the density. A suitable PDF for the reconstruction problem is the likelihood function for K independent normally distributed random variables [57],

$$\mathcal{L}(\mathbf{p}) = \prod_{i=1}^K \frac{1}{\sqrt{2\pi\eta_i^2}} \exp\left(-\frac{1}{2} \frac{(f_i(\mathbf{p}) - d_i)^2}{\eta_i^2}\right).$$

The maximum likelihood point estimator (MLE) is defined as

$$\mathbf{p}_{\text{MLE}} = \arg \max_{\mathbf{p}} \mathcal{L}(\mathbf{p}).$$

In cases where prior knowledge about the distribution of the model parameter exists, such as for example geometrical parameter constraints [17], one may also choose to instead maximize the full posterior probability density

$$\mathcal{P}(\mathbf{p}) \propto \pi(\mathbf{p}) \mathcal{L}(\mathbf{p}),$$

which is – up to a constant of proportionality – obtained by multiplying the prior probability density $\pi(\mathbf{p})$ with the likelihood function. The maximum a-posteriori point estimator (MAP)

$$\mathbf{p}_{\text{MAP}} = \arg \max_{\mathbf{p}} \mathcal{P}(\mathbf{p})$$

or the MLE are generally determined by means of a local optimization using methods such as the Nelder-Mead simplex algorithm or the gradient based L-BFGS-B method [17]. If the probability distribution exhibits multiple local minima, global heuristic optimization such as particle swarm optimization are employed [58]. In the context of scatterometry, it is often expensive to evaluate the model function. In this case, Bayesian optimization methods often significantly reduce the computational effort [31, 59].

Often, the magnitude of the variance η_i^2 is *a priori* unknown. However, it is often possible to define a realistic model for the variance and determine the most likely model parameters. A possible approach is to model the measurement variances for example as [41]

$$\eta_i^2(a, b, \mathbf{p}) = (a \cdot f_i(\mathbf{p}))^2 + b^2,$$

where one assumes that the error is composed of a background term b and a linear dependent noise, which could, e.g., stem from intensity-proportional power fluctuations of laser light. This can be incorporated into the parameter reconstruction simply by extending the parameter space of the respective PDFs, i.e. by considering the likelihood function

$$\mathcal{L}(a, b, \mathbf{p}) = \prod_{i=1}^K \frac{1}{\sqrt{2\pi\eta_i^2(a, b, \mathbf{p})}} \exp\left(-\frac{(f_i(\mathbf{p}) - d_i)^2}{2\eta_i^2(a, b, \mathbf{p})}\right).$$

An important information in the context of parameter reconstruction are not only the point estimates but also the confidence intervals of the parameter values. These are often given as the 16%, the 50% (median), and the 84% quantiles of the probability density distributions \mathcal{P} or \mathcal{L} . The quantiles can generally not be calculated in closed form, but are determined by drawing samples from the probability distribution using Markov chain Monte Carlo (MCMC) sampling techniques [58]. For stable quantile estimates often more than 10,000 samples are required.

B Weighted least-squares

The problem of finding the MAP or MLE, as defined in Appendix A, can in principle be transformed into that of solving a weighted least-square problem. Two assumptions go into this. First, when attempting to find the MAP the prior is sufficiently flat, such that it may be neglected. The logarithm of the posterior probability density $\mathcal{P}(\mathbf{p})$ is then up to a constant addition equal to the logarithm of the likelihood $\mathcal{L}(\mathbf{p})$, i.e. $\log \mathcal{P}(\mathbf{p}) = \text{const.} + \log \mathcal{L}(\mathbf{p})$. And second, a good approximation of the individual error variances exists. We assume that the relative error variances η_i^2/η_j^2 are known, but all of them may be over- or underestimated. We can then write

$$-2 \log \mathcal{P}(\mathbf{p}) + \text{const.} = \sum_{i=1}^K \frac{(f_i(\mathbf{p}) - d_i)^2}{\eta_i^2} = (\mathbf{f}(\mathbf{p}) - \mathbf{d})^T \mathbf{W} (\mathbf{f}(\mathbf{p}) - \mathbf{d}) = \chi^2(\mathbf{p}), \quad (\text{S1})$$

where $\mathbf{W} = \text{diag}(1/\eta_1^2, \dots, 1/\eta_K^2)$ is a diagonal matrix containing the error variances. Solving the least-square problem, i.e. finding the \mathbf{p} that minimizes Equation (S1), is therefore equivalent to finding the MAP or MLE. This can be efficiently done using, e.g., the Gauss-Newton method [3, 60] or the Levenberg-Marquardt algorithm [1, 2, 60].

The approaches work by determining at each iteration m at position \mathbf{p}_m a linear approximation of the model function

$$\mathbf{f}(\mathbf{p}_m + \boldsymbol{\delta}) \approx \mathbf{f}(\mathbf{p}_m) + \mathbf{J}\boldsymbol{\delta}, \quad (\text{S2})$$

where \mathbf{J} is the Jacobian matrix with entries $\mathbf{J}_{ij} = \partial f_i(\mathbf{p}) / \partial p_j|_{\mathbf{p}=\mathbf{p}_m}$. The derivative of χ^2 with respect to the step size $\boldsymbol{\delta}$ vanishes in the linear approximation for $\boldsymbol{\delta}_{\text{GN}}$ fulfilling

$$(\mathbf{J}^T \mathbf{W} \mathbf{J}) \boldsymbol{\delta}_{\text{GN}} = \mathbf{J}^T \mathbf{W} [\mathbf{d} - \mathbf{f}(\mathbf{p}_k)].$$

This Gauss-Newton step $\mathbf{p}_{m+1} = \mathbf{p}_m + \boldsymbol{\delta}_{\text{GN}}$ can be misleading, if it is larger than the validity range of the linear approximation of $\mathbf{f}(\mathbf{p})$. A more conservative approach is to make a small step in the direction of the gradient $\nabla \chi^2(\mathbf{p})$. The Levenberg-Marquardt algorithm [1] with improvements by R. Fletcher [47] aims to combine both strategies by introducing a damping factor λ that is adjusted according to the success of previous optimization steps and solving the equation

$$(\mathbf{J}^T \mathbf{W} \mathbf{J} + \lambda \cdot \text{diag}[\mathbf{J}^T \mathbf{W} \mathbf{J}]) \boldsymbol{\delta}_{\text{LM}} = \mathbf{J}^T \mathbf{W} [\mathbf{d} - \mathbf{f}(\mathbf{p}_k)].$$

The Levenberg-Marquardt algorithm is typically able to find the minimum of χ^2 with fewer iterations than other local optimization methods like the Nelder-Mead downhill-simplex approach or L-BFGS-B. This is because the Levenberg-Marquardt algorithm uses a linear model of *each* channel $f_i(\mathbf{p})$ resulting in an accurate local *second-order* model of χ^2 . On the other hand, L-BFGS-B uses an accurate local first-order model of χ^2 and only builds up an averaged approximation of the second-order Hessian matrix $(\mathbf{H})_{ij} = \frac{1}{2} \frac{\partial^2 \chi^2}{\partial p_i \partial p_j}$ during the minimization. It can be therefore beneficial to solve the weighted least square problem instead of maximizing the full posterior probability distribution $\mathcal{P}(\mathbf{p})$.

Under the assumption that the linear approximation of Equation (S2) is valid in a sufficiently large region around the minimum of χ^2 , it is possible to determine the confidence intervals of each parameter analytically by the diagonal elements of the parameter covariance matrix $\text{Cov}(\mathbf{p}_{\text{MLE}}) = \mathbf{H}^{-1} \approx (\mathbf{J}^T \mathbf{W} \mathbf{J})^{-1}$ [28, 27]. A possible over or underestimation of the measurement errors η_1, \dots, η_K in the weight matrix \mathbf{W} can be accounted for by a scaling with the regression standard error [28, 26]

$$\text{RSE} = \sqrt{\frac{\chi^2(\mathbf{p}_{\text{MLE}})}{K - N}}.$$

Recall that the regression standard error can be used to indicate how well the error variances were estimated. Assuming a correct model $\text{RSE} < 1$ indicates that the measurement uncertainties were overestimated and $\text{RSE} > 1$ that the measurement uncertainties were underestimated. The measurement uncertainties for the parameters p_i for $i = 1, \dots, N$ evaluate to

$$\epsilon_{p_i} = \text{RSE} \sqrt{(\text{Cov}(\mathbf{p}_{\text{MLE}}))_{ii}}.$$

C Derivation of the effective degrees of freedom \tilde{K}

In the main manuscript the probability distribution for the value of $\chi^2(\mathbf{p})$ given K Gaussian process (GP) predictions is approximated by a non-central chi-squared distribution with K degrees of freedom and a subsequent transformation to a Gaussian distribution. While K is usually chosen to be the number of data channels, we

define the *effective* number of degrees of freedom to be a number \tilde{K} that when used as a parameter of the probability distribution maximizes the probability density of all M observations $\mathbf{Y} = [\chi^2(\mathbf{p}_1), \dots, \chi^2(\mathbf{p}_M)]^T$ of the model function \mathbf{f} , i.e.

$$\tilde{K} = K_{\text{MLE}} = \arg \max_K \mathcal{L}(K; \mathbf{Y}),$$

where \mathcal{L} is the predictive distribution obtained by approximating the generalized chi-squared distribution for \mathbf{Y} twice, as described in the main manuscript. It is obtained by minimizing the logarithmic likelihood $\log \mathcal{L}$ with respect to the degrees of freedom. Since expressions for the PDF are involved and its values expensive to calculate [35, 36], we opt to find an approximation and minimize its logarithm instead.

In order to construct the approximate PDF, we first calculate

$$\chi_{\text{all}}^2 = \sum_m^M \chi^2(\mathbf{p}_m) = \sum_m^M \sum_k^K \frac{(f_{mk} - d_k)^2}{\eta_k^2}, \quad (\text{S3})$$

where $f_{mk} = f_k(\mathbf{p}_m)$ is the k -th component of the model function evaluated using the model parameter \mathbf{p}_m , d_k denotes the k -th component of the experimental data, and η_k^2 denotes the associated experimental noise variance. The sum can be formulated as a standard scalar product,

$$\chi_{\text{all}}^2 = \boldsymbol{\xi}^T \boldsymbol{\xi},$$

where

$$\boldsymbol{\xi} = \left(\frac{f_{11} - d_1}{\eta_1}, \dots, \frac{f_{M1} - d_1}{\eta_1}, \frac{f_{12} - d_2}{\eta_2}, \dots, \frac{f_{MK} - d_K}{\eta_K} \right)^T$$

is a vector of length MK and follows a multivariate normal distribution,

$$\boldsymbol{\xi} \sim \mathcal{N}(\boldsymbol{\mu}, \mathbf{M}), \quad \text{with } \boldsymbol{\mu} \in \mathbb{R}^{MK}, \mathbf{M} \in \mathbb{R}^{MK \times MK}.$$

Using the Kronecker product, the expectation value $\boldsymbol{\mu}$ of the vector can be expressed as

$$\boldsymbol{\mu} = \left(\frac{\mu_1 - d_1}{\eta_1}, \frac{\mu_2 - d_2}{\eta_2}, \dots, \frac{\mu_K - d_K}{\eta_K} \right) \otimes \mathbf{1}_{M \times 1}.$$

Here, μ_1, \dots, μ_K are the mean values of the GPs. The matrix \mathbf{M} describes the covariance between the components of the vector $\boldsymbol{\xi}$. Since channels are assumed to be uncorrelated, and only correlations between observations are considered, \mathbf{M} is block-diagonal,

$$\mathbf{M} = \text{diag} \left(\left(\frac{\sigma_1^2}{\eta_1^2} \mathbf{M}_1 \right), \left(\frac{\sigma_2^2}{\eta_2^2} \mathbf{M}_2 \right), \dots, \left(\frac{\sigma_K^2}{\eta_K^2} \mathbf{M}_K \right) \right).$$

Here $\sigma_1^2, \dots, \sigma_K^2$ are the variances of the GPs, such that $\mathbf{K}_i = \sigma_i^2 \mathbf{M}_i$ is the covariance matrix of the i -th GP and \mathbf{M}_i are the *unscaled* covariance kernel matrices. For the resource reasons discussed in the BTVO section of the main manuscript, we assume that the \mathbf{M}_i are shared between channels, such that $\mathbf{M}_i = \mathbf{M}_0$, and therefore

$$\mathbf{M} = \text{diag} \left(\left(\frac{\sigma_1^2}{\eta_1^2} \right), \left(\frac{\sigma_2^2}{\eta_2^2} \right), \dots, \left(\frac{\sigma_K^2}{\eta_K^2} \right) \right) \otimes \mathbf{M}_0.$$

Since the matrix \mathbf{M}_0 is unscaled, its variance entries on the diagonal are equal to 1. To see this, recall from the main manuscript that for a single Gaussian process we have

$$(\mathbf{K}_0)_{ij} = k(\mathbf{p}_i, \mathbf{p}_j) \quad \text{and} \quad k(\mathbf{p}, \mathbf{p}') = \sigma_0^2 \left(1 + \sqrt{5}r + \frac{5}{3}r^2 \right) \exp \left(-\sqrt{5}r \right), \quad \text{with } r = \sqrt{\sum_{i=1}^N \frac{(p_i - p'_i)^2}{l_i^2}}.$$

For the diagonal elements of \mathbf{K}_0 we have $\mathbf{p}_i = \mathbf{p}_j$, and $r = 0$, such that $k(\mathbf{p}, \mathbf{p}) = \sigma_0^2$, which means that the diagonal elements of the unscaled covariance matrix are equal to 1.

Analogous to Matsui et al., Equation (S3) is expressed as a linear combination of squared independent Gaussian random variables [11]. To do this, $\boldsymbol{\xi}$ is transformed into a standard normal,

$$\mathbf{g} = \mathbf{M}^{-1/2}(\boldsymbol{\xi} - \boldsymbol{\mu}) \sim \mathcal{N}(\mathbf{0}, \mathbf{1}_{MK}),$$

and \mathbf{M} is eigendecomposed as

$$\mathbf{M} = \mathbf{P}^T \mathbf{Y} \mathbf{P},$$

with eigenvectors

$$\mathbf{P} = \mathbf{1}_K \otimes \mathbf{P}_{\mathbf{M}_0},$$

where $\mathbf{P}_{\mathbf{M}_0}$ are the eigenvectors of the \mathbf{M}_0 matrix, and the associated eigenvalues are

$$\mathbf{Y} = \text{diag}(\boldsymbol{\lambda}) \quad \text{with} \quad \boldsymbol{\lambda} = \left(\frac{\sigma_1^2}{\eta_1^2}, \dots, \frac{\sigma_K^2}{\eta_K^2} \right) \otimes \boldsymbol{\lambda}_{\mathbf{M}_0}.$$

Using these definitions

$$\begin{aligned} \chi_{\text{all}}^2 &= \left(\mathbf{g} + \mathbf{M}^{-1/2} \boldsymbol{\mu} \right)^T \mathbf{M} \left(\mathbf{g} + \mathbf{M}^{-1/2} \boldsymbol{\mu} \right) = \left(\mathbf{P}\mathbf{g} + \mathbf{P}\mathbf{M}^{-1/2} \boldsymbol{\mu} \right)^T \mathbf{Y} \left(\mathbf{P}\mathbf{g} + \mathbf{P}\mathbf{M}^{-1/2} \boldsymbol{\mu} \right) \\ &= (\mathbf{u} + \mathbf{b})^T \text{diag}(\boldsymbol{\lambda}) (\mathbf{u} + \mathbf{b}) = \sum_i^{MK} \lambda_i (u_i + b_i)^2 = \sum_i^{MK} r_i^2, \end{aligned}$$

where now $r_i \sim \mathcal{N}(\sqrt{\lambda_i} b_i, \lambda_i)$. To parameterize the distribution, the eigenvalues of the \mathbf{M} matrix and the vector \mathbf{b} is decomposed as

$$\mathbf{b} = \mathbf{P}\mathbf{M}^{-1/2} \boldsymbol{\mu} = \left(\frac{\mu_1 - d_1}{\sigma_1}, \dots, \frac{\mu_K - d_K}{\sigma_K} \right) \otimes \left(\mathbf{P}_{\mathbf{M}_0} \mathbf{M}_0^{-1/2} \mathbf{1}_{M \times 1} \right) = \mathbf{b}_1 \otimes \mathbf{b}_2.$$

Due to the non-unit variances λ_i , χ_{all}^2 follows a *generalized* chi-squared distribution. By following the steps taken by Uhrenholt and Jensen in renormalizing χ_{all}^2 [12], we can transform the distribution into an approximate *non-central* chi-squared distribution. The scaling factor for this is the square root of the mean variance, i.e.

$$\gamma = \sqrt{\frac{1}{MK} \sum_i^{MK} \lambda_i} = \sqrt{\frac{1}{K} \sum_k^K \frac{\sigma_k^2}{\eta_k^2}} \sqrt{\frac{1}{M} \sum_m^M (\boldsymbol{\lambda}_{\mathbf{M}_0})_m} = \sqrt{\frac{1}{K} \sum_k^K \frac{\sigma_k^2}{\eta_k^2}}.$$

For the last step, we use that the sum over the eigenvalues of the matrix \mathbf{M}_0 is equal to its trace, which equates to the number of observations M since \mathbf{M}_0 is a covariance matrix with unit variances. Each of the components of χ_{all}^2 is scaled with γ^2 , i.e. $\chi_{\text{all}}^2 \rightarrow \chi_{\text{ren}}^2 = \gamma^{-2} \chi_{\text{all}}^2$. This then yields

$$\gamma^{-2} \chi_{\text{all}}^2 = \sum_i^{MK} s_i^2 \quad \text{with} \quad s_i \sim \mathcal{N}(\sqrt{\gamma^{-2} \lambda_i} b_i, \gamma^{-2} \lambda_i).$$

With $\gamma^{-2} \lambda_i \approx 1$ we therefore assume that $\gamma^{-2} \chi_{\text{all}}^2$ approximately follows a non-central chi-squared distribution, which is parameterized with $V = MK$ degrees of freedom and a non centrality parameter

$$\kappa = \gamma^{-2} \sum_i^{MK} \lambda_i b_i^2 = \gamma^{-2} \left(\sum_{i=1}^M (\boldsymbol{\lambda}_{\mathbf{M}_0})_i (\mathbf{b}_2)_i^2 \right) \left(\sum_{i=1}^K \frac{\sigma_i^2}{\eta_i^2} \frac{(\mu_i - y_i^*)^2}{\sigma_i^2} \right) = \gamma^{-2} M \sum_i^K \frac{(\mu_i - d_i)^2}{\eta_i^2}.$$

For the last step of the previous equation we use the following identity

$$\begin{aligned} \sum_{i=1}^M (\boldsymbol{\lambda}_{\mathbf{M}_0})_i (\mathbf{b}_2)_i^2 &= \mathbf{b}_2^T \text{diag}(\boldsymbol{\lambda}_{\mathbf{M}_0}) \mathbf{b}_2 = \mathbf{1}_{1 \times M} \mathbf{M}_0^{-T/2} \underbrace{\mathbf{P}_{\mathbf{M}_0}^T \text{diag}(\boldsymbol{\lambda}_{\mathbf{M}_0}) \mathbf{P}_{\mathbf{M}_0} \mathbf{M}_0^{-1/2}}_{\mathbf{M}_0} \mathbf{1}_{M \times 1} \\ &= \mathbf{1}_{1 \times M} \underbrace{\mathbf{M}_0^{-T/2} \mathbf{M}_0 \mathbf{M}_0^{-1/2}}_{\mathbf{1}_{M \times M}} \mathbf{1}_{M \times 1} = M. \end{aligned}$$

This distribution is further approximated by means of a normal distribution where an approximation described by Sankaran [61] is employed, yielding the approximation of the likelihood function \mathcal{L} . In order to calculate the *effective* degrees of freedom of this distribution, we minimize the logarithm of the likelihood with respect to the total degrees of freedom V ,

$$\tilde{V} = V_{\text{MLE}} = \arg \min_V \log(\mathcal{L}(V; \gamma^{-2} \chi_{\text{all}}^2)),$$

where

$$\log(\mathcal{L}(V; \gamma^{-2} \chi_{\text{all}}^2)) = -\log(\varrho) - \frac{1}{2} \left(\frac{z - \alpha}{\varrho} \right)^2$$

and

$$\begin{aligned} z &= \left(\frac{\gamma^{-2} \chi_{\text{all}}^2}{V + \kappa} \right)^h, \quad \alpha = 1 + h(h+1) \left(\frac{r_2}{2r_1^2} - (2-h)(1-3h) \frac{r_2^2}{8r_1^4} \right), \quad \text{and} \\ \varrho &= h \frac{\sqrt{r_2}}{r_1} \left(1 - (1-h)(1-3h) \frac{r_2}{4r_1^2} \right) \quad \text{where} \quad h = 1 - \frac{r_1 r_3}{3r_2^2}. \end{aligned}$$

The first three cumulants of the non-central chi-squared distribution are given as

$$r_1(V) = V + \kappa, \quad r_2(V) = 2(V + 2\kappa), \quad \text{and} \quad r_3(V) = 8(V + 3\kappa).$$

A scaling factor s for the actual degrees of freedom for any observation is then derived by taking $s = V/\tilde{V}$, such that $\tilde{K} = K/s$.

We note that the scaling factor γ and the non-centrality κ do not depend on entries of the matrix \mathbf{M}_0 of the covariances between the data points. This means that every observed data point has the same weight for determining the effective degrees of freedom. As a consequence, the effective degrees of freedom generally decreases during the minimization of the chi-squared deviation, since small chi-squared values are more compatible with a smaller number of degrees of freedom. The smaller values has the advantage that it yields a more exploratory behavior once the BTVO algorithm has drawn many samples close to an identified local minimum. The effective degree of freedom calculated based on a set of uniformly distributed samples of the complete parameter space, will generally have a larger value that is more representative to the measurement process itself.

D MCMC sampling of all parameters of the likelihood function of the MGH17 dataset

Figure S1 shows a comparison of the results of MCMC sampling of the likelihood functions of the MGH17 dataset, and completes the excerpts shown in the main manuscript. The top image shows the results of sampling the model function directly, the bottom image shows the results of sampling a trained surrogate model of the model function. In addition to the five model parameters β_1 to β_5 , an error model scaling parameter η_c is shown. A discussion is found in the main manuscript.

E Comparison of GIXRF fit results and experimental values

In Figure S2 the output of the model at the optimized reconstructed parameter value \mathbf{p}_{MLE} is shown in comparison to the experimental observations. As the model output and the experimental observations in the top image are indistinguishable, the middle image shows the difference of the two datasets, relative to the experimental uncertainties. In order to highlight the quality of the fit, the experimental uncertainties are highlighted as a green shaded band centered around the zero-difference line. The bottom image finally shows a histogram of the normalized differences of the middle image, overlaid with a (scaled) Gaussian fit. As reference, the experimental uncertainty band is again shown as a shaded green band.

Most of the outputs of the optimized model function are within the uncertainties of the experimental observations. This is reflected in the Gaussian fit of the histogram of the normalized differences, which has distribution parameters mean $\mu = -0.012$ and standard deviation $\sigma = 0.81$.

F MCMC sampling of the approximate likelihood function of the GIXRF dataset

Using the surrogate augmented MCMC method we have sampled the approximate likelihood function of the GIXRF dataset. An excerpt of the results is shown in Figure S3, where we have limited the displayed parameters to the critical dimension cd , the scaling parameter s_N , and the offset of the incidence angle θ . For these parameters we observe correlations at the reconstructed parameter value \mathbf{p}_{MLE} . This is due to the fact that the right-most maximum in the measurement data, c.f. e.g. Figure S2 at approximately 89° , is strongly correlated to the critical dimension cd [44]. A change in the offset angle Δ_θ moves the peak, which leads to a correlation between cd and Δ_θ . The correlation between s_N and cd can be explained if we consider, that a larger critical dimension means that the grating contains more material, which increases the fluorescence signal. s_N is the parameter that scales this signal to match the experimentally observed one. In order to still match the experimental measurement when increasing the critical dimension, the fluorescence signal has to be scaled down.

The remaining model parameters show only minor correlations.

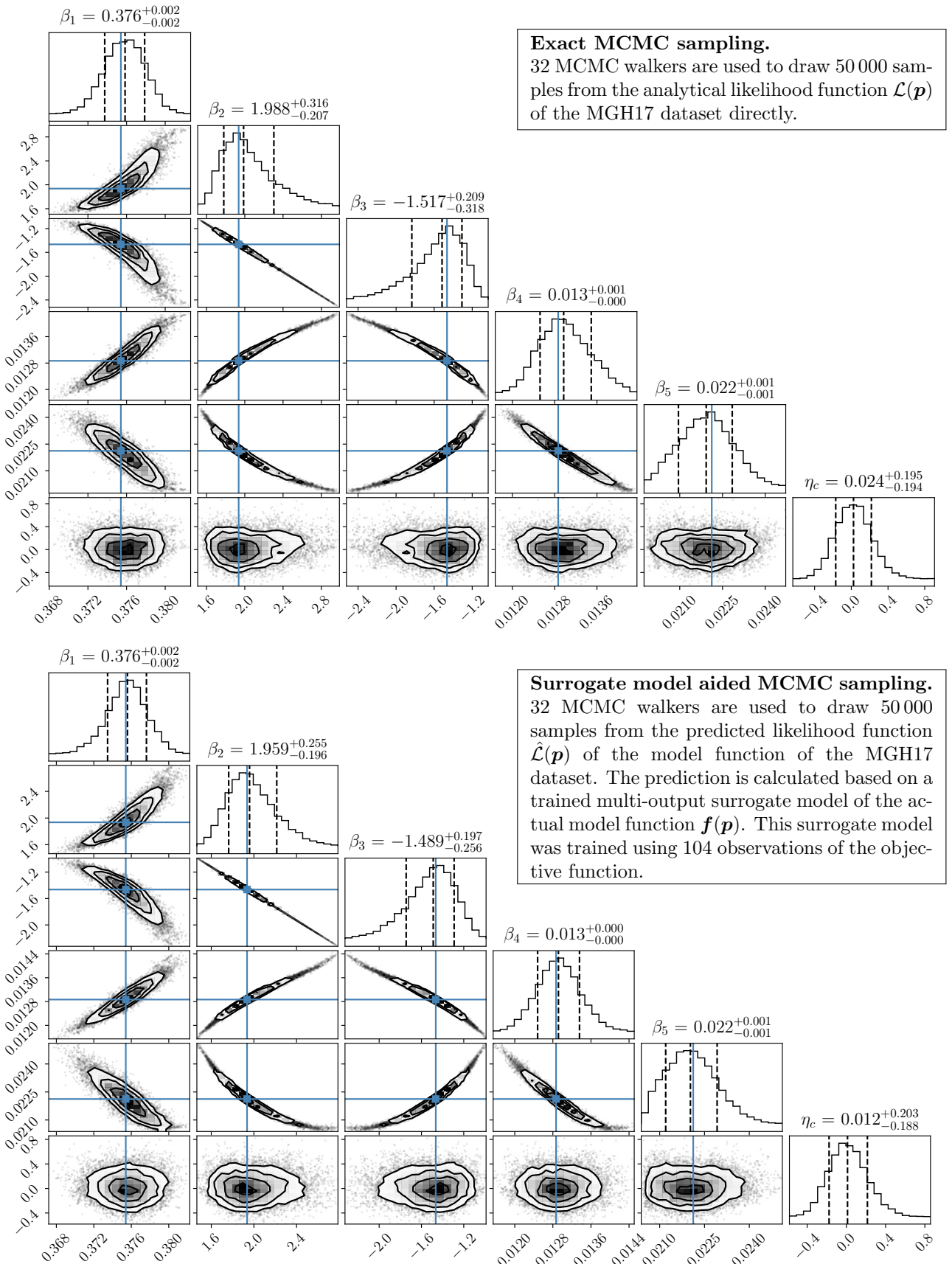


Figure S1: The results of MCMC sampling of the likelihood function of the MGH17 dataset, using the exact likelihood function (left) directly and using a trained multi-output surrogate model (right) to calculate a stochastic prediction of the likelihood function. A direct comparison of the two results reveals that the surrogate model approach is capable of reproducing the model parameter distributions as well as revealing correlations between the individual model parameters, while using significantly fewer evaluations of the model function. The blue lines shown are the certified NIST results [45].

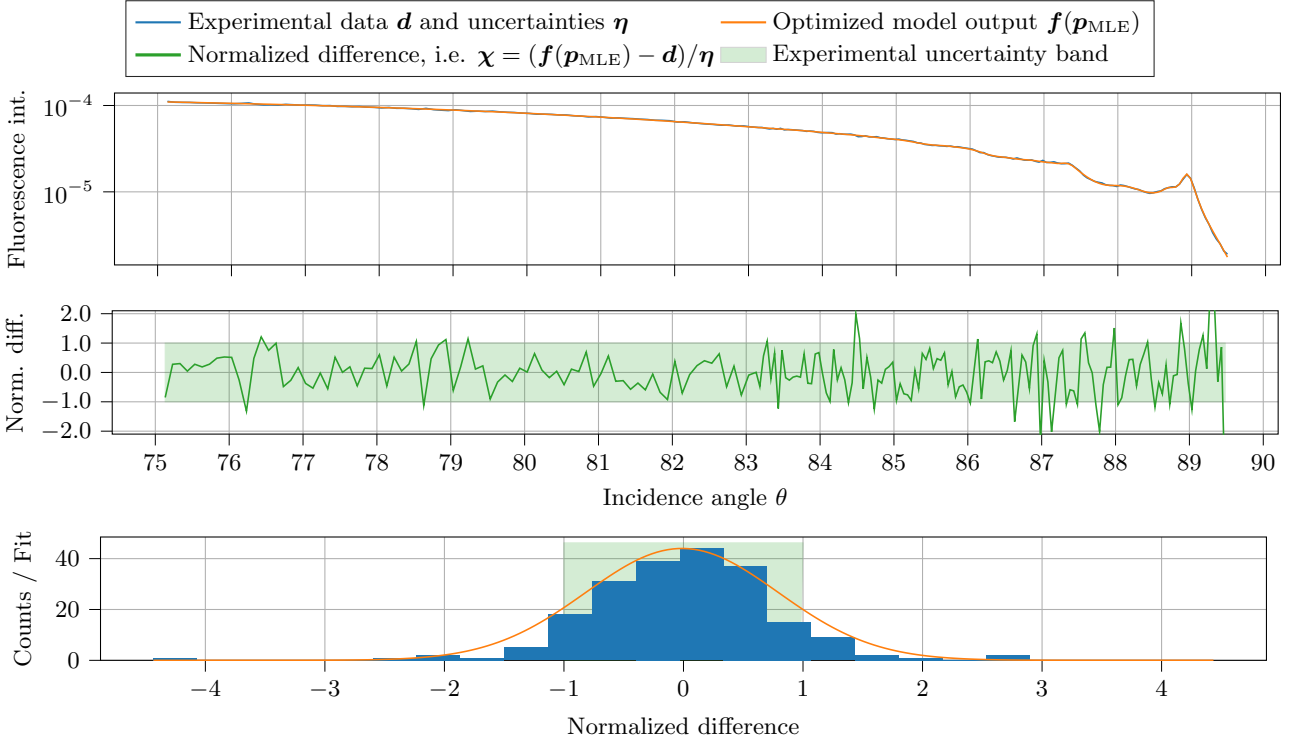


Figure S2: A comparison of the optimized model results $f(\mathbf{p}_{\text{MLE}})$ and the GIXRF experimental data \mathbf{d} . Due to the quality of the fit, the experimental data and the optimized model results are indistinguishable. The measurement uncertainty η is approximately two orders of magnitude smaller than the experimental data, and is therefore indiscernible in the top image. The middle image shows the difference of the model outputs and experimental measurements, normalized to the measurement uncertainty. The measurement uncertainty is shown as a green bar. The bottom image shows a histogram of the relative differences of the middle image, overlaid with a (scaled) Gaussian fit of the histogram data.

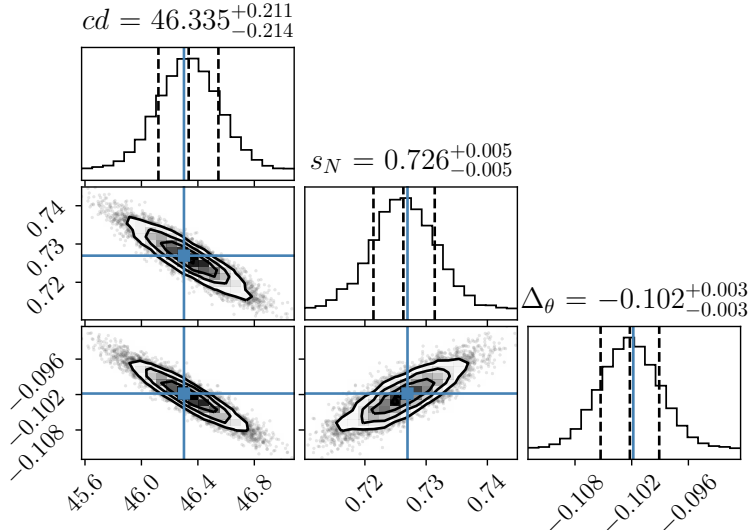


Figure S3: The approximate likelihood function of the GIXRF dataset was sampled using the surrogate augmented MCMC method. The displayed parameters are limited to the critical dimension cd , the scaling parameter s_N , and the offset of the incidence angle θ . For these parameters we observe correlations at the reconstructed parameter value \mathbf{p}_{MLE} . The blue lines are the results of the parameter reconstruction.